BRNO UNIVERSITY OF TECHNOLOGY

VYSOKÉ UČENÍ TECHNICKÉ V BRNĚ

FACULTY OF MECHANICAL ENGINEERING

FAKULTA STROJNÍHO INŽENÝRSTVÍ

INSTITUTE OF MATERIALS SCIENCE AND ENGINEERING

ÚSTAV MATERIÁLOVÝCH VĚD A INŽENÝRSTVÍ

RADIATION-INDUCED DAMAGE IN BAFFLE-BOLTS OF PWR REACTOR VESSEL INTERNALS

RADIACÍ INDUKOVANÉ POŠKOZENÍ VE ŠROUBECH VNITŘNÍ VESTAVBY PWR REAKTORŮ

SHORT VERSION OF DOCTORAL THESIS

TEZE DIZERTAČNÍ PRÁCE

AUTHOR — **Ing. Jan Michalička**

AUTOR PRÁCE

SUPERVISOR — **prof. Ing. Rudolf Foret, CSc.**

ŠKOLITEL

BRNO 2024

Abstract

The doctoral thesis deals with the transmission electron microscopy of radiation damage in austenitic stainless steels of baffle bolts of PWR core internals, where the damage is induced by a high flux neutron irradiation at high temperatures and can lead to aging issues of the bolts in the form of IASCC. Therefore, the study encompasses evolution of the radiation damage microstructure and microchemistry and the influence of changes in irradiation variables (temperature, dose rate, neutron spectrum). An important part of the thesis is self-ion irradiation for emulation of high dose neutron damage in the bolts corresponding to the PWR lifetime extension to 60+ years.

Significant gradients of irradiation temperature (~270 °C in the bolt head and ~400 °C in the bolt's shank due to gamma heating) and neutron dose rate are expected along the baffle bolts. Therefore, the influence of these gradients on the radiation damage microstructure was assessed in three positions along a shank of a baffle bolt made of 08Ch18N10T steel irradiated to a dose of 11.4 dpa under the in-service conditions of a decommissioned WWER-440 reactor. A synergistic effect of increasing temperature and decreasing dose rate was observed in the form of a significant increase in average size and decrease in density of cavities and higher abundance of radiation-induced precipitates. The gradients did not cause differences in the population of Frank dislocation loops and in radiation hardening of the bolt.

The influence of the neutron spectrum on IASCC susceptibility was investigated on CW 316 steel irradiated in an experimental reactor at 300 °C to dose of 15 dpa in positions with fast neutron flux (with Hf shielding of thermal neutrons) or with fast and thermal neutron fluxes (PWR-like mixed spectrum). The TEM revealed very similar measures of Frank dislocation loops and radiation-induced precipitates after both irradiations, but a significantly higher density of nano-cavities, cavity denuded zones along grain boundaries and cavities at grain boundaries after the mixed spectrum irradiation. The observed cavity microstructure is consistent with the higher He production rate of the mixed spectrum and it suggests correlation of helium production rates with IASCC susceptibility. This is further supported by SSRT tests, which revealed higher IASCC susceptibility of specimens irradiated by mixed spectrum.

5 MeV Ni^{++} or Fe^{++} ion irradiations of CW 316 to 23 dpa and 130 dpa at 380 °C, 23 dpa at 500 °C, and 15 dpa at 600 °C were performed to emulate microstructure and microchemistry (RIS) of the radiation damage as produced fast neutrons in BOR-60 reactor in the same heat of material at 320 °C and doses up to 46 dpa. For the first time, it is demonstrated, that all types of the neutron radiation damage in the CW 316 could be successfully emulated by single self-ion irradiations, particularly at 380 °C. Although this temperature was calculated by Mansur's invariant equations to match the microstructure and temperature 600 °C to match the microchemistry, despite a large difference in dose rates, $\sim 10^{-3}$ dpa/s (self-ions) and $\sim 5 \times 10^{-7}$ dpa/s (fast neutrons), a relatively small temperature shift of 60 °C was sufficient to emulate all complex radiation damage. This indicates a large influence of the high sink density of the cold-worked material and that the sink density is a critical factor in determining temperature shifts for successful self-ion emulation of neutron irradiations.

Key words

Radiation-induced damage, transmission electron microscopy, PWR baffle bolts, neutrons, self-ions.

Abstrakt

Tato disertační práce se zabývá transmisní elektronovou mikroskopií radiačního poškození ve šroubech z austenitických nerezových ocelích používaných ve vnitřní vestavbě tlakovodních reaktorů PWR, kde je poškození indukováno neutrony o vysokém toku a při vysokých teplotách a může vést k s rostoucí dávkou k poškození šroubů ve formě IASCC. Proto se studie zabývá vývojem mikrostruktury a mikrochemie radiačního poškození a vlivem změn v parametrech ozařování (teplota, dávková rychlost, spektrum neutronů). Důležitou částí práce je ozařování těžkými ionty emulujícími poškození ve šroubech po vysokých neutronových dávkách odpovídajících prodloužené životnosti PWR na 60+ let.

Významné teplotní gradienty ozařování (~270 °C v hlavičce šroubu a ~400 °C v dříku šroubu vlivem gama záření) a pokles dávkového příkonu neutronů jsou očekávány podél šroubů vestaveb. Vliv těchto gradientů na radiační poškození byl proto hodnocen pomocí TEM ve třech pozicích podél dříku šroubu z oceli 08Ch18N10T ozářeném dávkou 11.4 dpa za provozních podmínek vyřazeného reaktoru WWER-440. Byl zjištěn synergický efekt zvyšující se teploty a klesajícího dávkového příkonu neutronů ve formě významného zvýšení průměrné velikosti a snížení hustoty kavit a vyššího výskytu radiací indukovaných precipitátů. Tyto gradienty nezpůsobily změny v populaci Frankových dislokačních smyček a v radiačním zpevnění šroubu.

Vliv spektra neutronů na náchylnost k IASCC byl zkoumán na oceli CW 316 ozářené v experimentálním reaktoru při 300 °C na 15 dpa v pozicích s rychlým neutronovým tokem (s Hf stíněním tepelných neutronů) nebo s rychlým a tepelným neutronovým tokem (smíšené spektrum typické pro PWR). TEM analýza po obou ozářeních zjistila velmi podobné hodnoty Frankových dislokačních smyček a radiací indukovaných precipitátů, ale významně vyšší hustotu nano-kavit, ochuzené oblasti o kavity podél hranic zrn a vznik kavity na hranicích zrn po ozáření smíšeným spektrem. Pozorovaná mikrostruktura kavit souhlasí s vyšší produkcí helia při ozáření smíšeným spektrem a naznačuje korelaci míry produkce helia s náchylností oceli k IASCC. Toto je dále podpořeno SSRT testy, které odhalily vyšší náchylnost k IASCC vzorků ozářených smíšeným spektrem.

5 MeV Ni^{++} nebo Fe^{++} iontové ozařování oceli CW 316 na 23 dpa a 130 dpa při 380 °C, 23 dpa při 500 °C a 15 dpa při 600 °C bylo provedeno pro emulaci mikrostruktury a mikrochemismu radiačního poškození, které bylo vytvořeno ve stejném materiálu ozařováním rychlými neutrony v reaktoru BOR-60 při 320 °C a dávkách až 46 dpa. Poprvé bylo prokázáno, že všechny typy neutronového poškození v CW 316 byly úspěšně emulovány jediným ozařováním těžkými ionty, konkrétně při 380 °C. I když byla tato teplota vypočítána pomocí invariantních rovnic Mansura k emulaci mikrostruktury a teplota 600 °C k emulaci RIS, navzdory vysokému rozdílu v dávkových rychlostech, ~10^{-3} dpa/s (těžké ionty) a ~5×10^{-7} dpa/s (rychlé neutrony), byl relativně malý posun teploty o 60 °C postačující k emulaci mikrostruktury i mikrochemismu. To naznačuje velký vliv vysoké hustoty pastí bodových poruch materiálu tvářeného za studena a že tato hustota pastí je kritickým faktorem pro stanovení teplotních posunů pro úspěšnou emulaci neutronového ozařování pomocí těžkých iontů.

Klíčová slova

Radiací indukované poškození, transmisní elektronová mikroskopie, šrouby vnitřní vestavby PWR, neutrony, těžké ionty.

Contents

1 Introduction

Reactor vessel internal components (RVI) of pressurized-water reactors (PWR) are exposed to a harsh environment including a high-flux neutron irradiation at high temperatures reaching 400°C. The RVI are made predominantly from austenitic stainless steels [1] and the neutron irradiation at high temperatures induces changes in their original microstructure and microchemistry in form of complex radiation damage including extended radiation-induced defects and radiation-induced segregations (RIS) at lattice sinks [2]. Consequently, this process leads to degradation of mechanical properties of the RVI, manifested by increase in yield strength, loss of ductility and toughness [2-6]. During the reactor lifetime, the degraded RVI components exposed to the harsh corrosive environment of the pressurized cooling water may potentially subject material aging issues, particularly in the form of loss of integrity via irradiation-assisted stress corrosion cracking (IASCC) [7, 8]. This is depicted in **Figure 1-1**, where the IASCC has onset after an intermediate dose around 10 dpa (displacements per atom).

The evolution of the PWR radiation damage in austenitic stainless steels is a complex process in microstructure and microchemistry of the alloy, when point defects (interstitials and vacancies) induced in the crystal lattice form extended defects and solute segregations in volumes at atomic up to nano-metric scale. This complexity demonstrates **Figure 1-2**, where point defect clusters, dislocation loops, cavities and RIS at grain boundaries act as radiation damage with the important influence on the IASCC susceptibility.

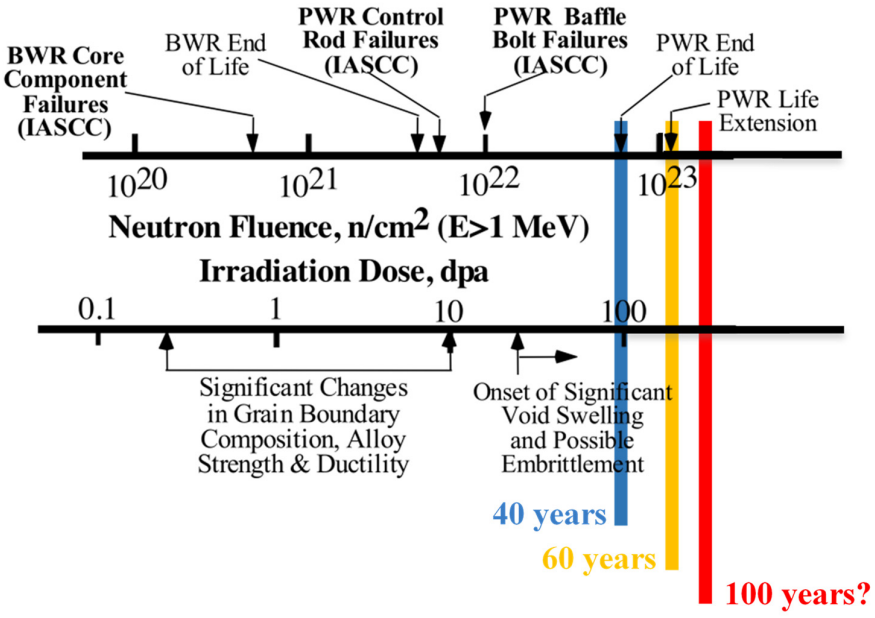

Figure 1-1: Propagation of relevant aging issues and microstructure degradation of RVIs to increasing irradiation time is shown in fluence and dose scale, respectively. Knowledge of the issues and microstructure degradation of components irradiated to high neutron doses equal to 40 years or beyond is missing. Adapted from [2].

In presence, the PWR license extensions are planned beyond the designed reactor lifetime to sustain cheap and carbon-free energy sources **[9, 10]**. A typical PWR lifetime is 40 years and the license renewals are planed to 60+ years, which means that the reactor components will have to withstand at least 50% longer operational period of time than considered the original license. Therefore, the attention is focused to RVI components with known ageing issues. It concerns particularly bolts of a baffle-to-former assembly (later named as baffle bolts) made from cold-worked (CW) austenitic stainless steels (SS). The baffle bolts are used in the core regions, where neutron fluxes and temperatures reach high values. It is estimated that baffle bolts can accumulate high neutron doses exceeding 100 dpa at the end of the 60-year operation **[1, 8]**.

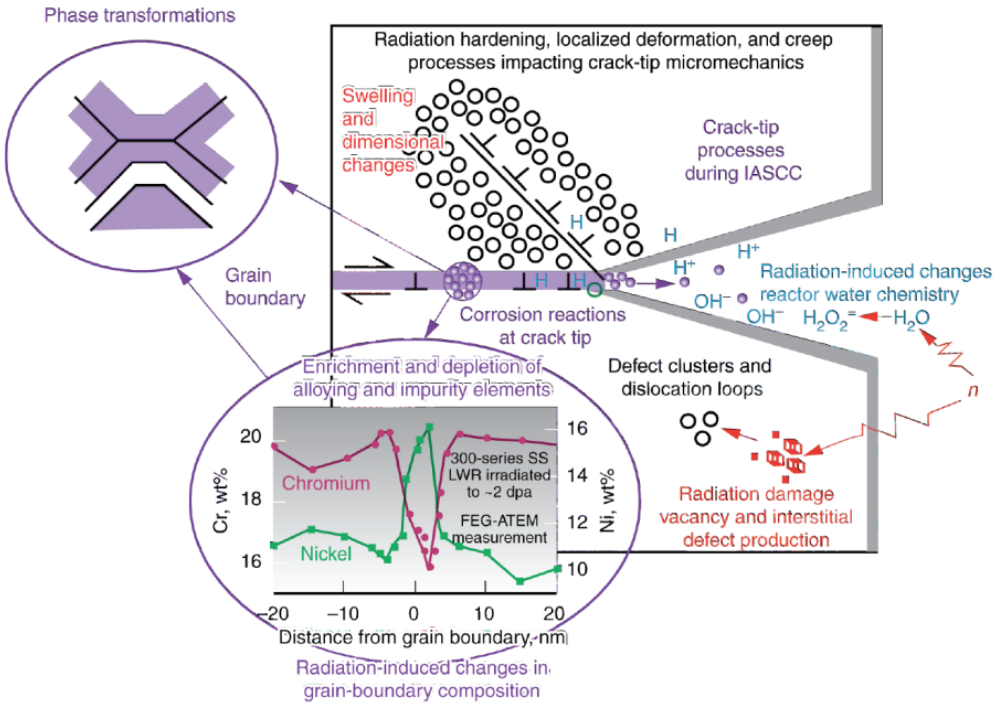

Figure 1-2: Schematic illustration of mechanistic issues of the radiation damage believed to influence crack propagation during IASCC of PWR austenitic stainless steels **[2]**.

Due to the limited reactors of this age, there is a lack or very limited amount of available material from PWR baffle bolts irradiated to the high neutron doses, and hence the data and knowledge of the high dose neutron radiation damage and connected aging issues is limited too. Therefore, investigations of baffle bolts extracted from a PWR after low to intermediate doses are vital to obtain the necessary understanding about the trends of radiation damage evolution and to find out correlations between the radiation damage and the IASCC susceptibility. The knowledge obtained from neutron irradiated RVI components extracted from commercial reactors is generally unique and with a high impact for the research community. An important

example are studies done on Tihange baffle bolts **[11, 12]**. A comprehensive investigation was performed on baffle bolts obtained within a unique project aimed to assess complex characteristics of RVI components from core shroud segments of a WWER-440/230 type reactor (eastern design of a PWR) from Greifswald decommissioned after 15 years of operation resulting in a dose of 11.4 dpa. The transmission electron microscopy (TEM) was conducted to address effects of irradiation temperature and dose rate gradients along the bolt on the radiation damage evolution. This work was published in **[13, 14]** and it is a subject of the first objective of this thesis.

A possibility for high dose irradiations is the use of experimental high-flux reactors. They allow the 100 dpa irradiation time to be reduced from decades to years and a well-defined and controlled irradiation environment **[15]**. Extensive results on IASCC testing and microstructure of the high dose radiation damage of baffle bolt and other RVI materials come mainly from two research programs using fast breeder (FBR) and thermal reactors emulating the PWR environment: A Cooperative IASCC Research (CIR) program conducted by EPRI in USA, where higher doses up to 46 dpa at temperature of 320 °C were produced in a BOR-60 FBR **[16, 17]**, and a program conducted by Électricité de France (EDF), where irradiations in FBRs (BOR-60, EBR-II and Phenix) and thermal SM reactor, achieved doses up to the level of the PWR end of life (~ 95 dpa) at PWR-relevant temperatures (300–400 °C) **[18, 19]**. On the contrary, FBR and PWR irradiation variables differ, which can influence the material degradation and the IASCC susceptibility. Predominantly, Ni transmutations to He are significantly suppressed in the FBR spectra due to the missing thermal neutrons. It results in lower He production rates (~0.5 appm He/dpa for FBR spectrum and ~15 appm He/dpa for PWR spectrum **[4]**) and lower swelling rates under FBR irradiations. In order to verify the representativeness of the FBR irradiation on the IASCC susceptibility of RVI materials irradiated in PWR, microstructure and IASCC benchmarks between FBR and PWR irradiations have been conducted on a baffle bolt CW 316 SS at comparable irradiation doses and temperatures at Pacific Northwest National Laboratory using the BOR-60 reactor **[20]** and in the EDF program (Samara project) using the SM reactor **[19]**. The part of the Samara project was TEM investigation and benchmark of the CW 316 SS irradiated by thermalized and fast neutron spectra. This work was published in **[21]** and it is a subject of the second objective of this thesis.

Nevertheless, every neutron high dose irradiation is slow and every investigation of materials irradiated by neutrons is expensive, technically difficult and time consuming due to the high radioactivity of samples. All these restraints can be overcome by irradiations with heavy ion beams in an accelerator **[22, 23]**. The irradiation times can be reduced dramatically, when 100 dpa can be accumulated in one day. The ion accelerators have well controlled experimental conditions and allow to study effects of individual irradiation variables. Irradiated samples are not activated and thus can be studied without any safety restrictions. Despite the advantages above neutrons, several aspects of the heavy ion irradiations must be considered. It is penetration depth of heavy ions limited to few hundreds of nm, which limits mechanical testing and requires focused ion beam (FIB) sample preparation for TEM. Heavy ions do not

cause transmutations of solute elements to He, but the missing He production can be emulated by pre-implantation. Both neutrons and heavy ions produce similar collision cascades and thus they have similar probability of point defect recombination during cascade quench **[24]**. However, heavy ions with high dose rate may influence evolution of some radiation-induced phases common for neutron irradiations due to the ballistic mixing effect **[25]**. And importantly, substantially different dose rates, 10^{-9}–10^{-7} dpa/s for a PWR core **[26]** vs. ~10^{-3} dpa/s for heavy ions, cause a fundamental change in the fate of point defects and the subsequent evolution of the radiation-induced microstructure and segregation at point defect sinks at a given dose and temperature **[27]**. Considering these factors, two vital actions are needed to tailor the heavy ion irradiation experiment successfully. First, to establish target dose and temperature of accelerated irradiation to compensate differences from the native neutron irradiation. These parameters can be evaluated using the invariance equations derived by Mansur **[27]**. Typically, the higher dose rate is compensated by higher temperature and/or dose. Second, to benchmark microstructure and microchemistry of the radiation damage in the same heat of material irradiated under both native and accelerated conditions to validate the established ion irradiation conditions. Benchmarks should evaluate all types of radiation damage which co-evolve during the neutron irradiation. Materials for benchmarks have to meet two criteria: 1) they must have undergone high-dose neutron irradiation and been characterized, and 2) archive material from the same heat that was irradiated must be available in sufficient quantities for ion irradiations. Successful comparative in-reactor and heavy ion irradiation experiment has been already conducted on an identical heat of a ferritic–martensitic steel HT9 irradiated by neutrons to 155 dpa at 443 °C and by 5 MeV Fe^{++} ions combined with He pre-implantation **[28, 29]**. The target heavy ion irradiation parameters, established by Mansur's equations, were 188 dpa at temperature 460 °C. In this thesis, a successful emulation of microstructure and microchemistry of the radiation damage is demonstrated via the benchmark of TEM data from the same heat of a baffle bolt CW 316 SS irradiated by fast neutrons in BOR-60 to doses up to 46 dpa at 320 °C **[16, 17]** and by single 5 MeV Fe^{++} or Ni^{++} ion irradiations to 23 dpa or 130 dpa at 380 °C. This work was published in **[30- 32]** and it is a subject of the third objective of this thesis.

The modern TEMs allow to characterize the radiation damage in terms of morphology, crystallography and chemical composition as a single experimental instrument and with a sufficient lateral resolution in the order of 0.1 nm. **[33-35]**. Therefore, they are the most versatile tool for the radiation damage characterization and their high analytical power paves the way for novel characterization techniques of the radiation damage at sub-nanometric scale. Since this study was based on TEM investigation of the radiation damage induced by neutrons or heavy ions, the emphasis was always placed strongly to optimize each used microscopy technique. This resulted in development of new methodologies for TEM investigation of the complex radiation damage including novel corelative microscopy techniques allowed by the used state-of-the-art microscope TITAN Themis. Aside of the outcomes related to the established objectives, the new TEM methodologies are important results and they are surveyed in the experimental part of the main document of this thesis (later as "*the main document*").

2 Objectives of the thesis

With respect to the present knowledge and own experimental work of the studied subject of the radiation-induced damage in PWR baffle bolts, the main objectives established for this thesis are summarized in the following points:

1. To perform TEM analysis of radiation-induced defects (Frank loops, radiation-induced precipitates and cavities) in a PWR baffle bolt irradiated by neutrons in a commercial PWR nuclear reactor.

   To evaluate effects of irradiation conditions (i.e. temperature, dose and dose rate) and their gradients on the radiation damage along the baffle bolt shank.

2. To perform TEM analysis of radiation-induced defects (Frank loops, radiation-induced precipitates and cavities) in a PWR baffle bolt material experimentally irradiated under different neutron spectra emulating FBR neutron spectrum and PWR mixed spectrum.

   To evaluate effects of fast and mixed neutron spectra on radiation damage microstructure.

3. To perform a self-ion irradiation experiment emulating a high dose neutron radiation damage in a PWR baffle bolt material.

   To perform S/TEM analysis of radiation damage affecting radiation hardening and IASCC (i.e. radiation-induced defects and RIS at grain boundaries) in the self-ion irradiated material.

   To evaluate effects of self-ion irradiation conditions used in the performed irradiation experiment.

   To benchmark obtained S/TEM results with S/TEM results from the same heat of the material irradiated to referential high doses by neutrons in an FBR and to validate the used conditions for emulation of the neutron irradiation.

3 Baffle bolt irradiated in a commercial PWR reactor

3.1 Experimental

The investigated material was a neutron irradiated baffle bolt extracted from a WWER-440/230 type reactor of nuclear power plant Greifswald, Unit 1, decommissioned after 15 years of operation. The bolt was a part of a baffle-former-barrel assembly from extracted shroud and it was made from a Ti-stabilized austenitic stainless steel 08Ch18N10T (equivalent to AISI 321 SS). The exact thermo-mechanical treatment of the material and manufacturing process of the bolt is not known. A nominal chemical composition of the steel is in **Table 3.1-1**. A real chemical composition of the extracted samples was technically impossible to measure due to high radioactivity of the material. Archive non-irradiated material had not been at disposal. The bolt was about 30 mm long and 12 mm in diameter, the shank comprises of 10 – 11 threads.

Table 3.1-1: The required chemical composition for the 08Ch18N10T austenitic stainless steel, in wt. % **[13]**.

C	Mn	Si	P	S	Cu	Ni	Cr	Ti	Co	N
Max 0.08	Max 2.0	Max 0.8	Max 0.035	Max 0.02	Max 0.30	9.0 – 11.0	17.0 – 19.0	Min 5xC Max 0.70	Max 0.05	Max 0.05

The maximum fluence obtained by the baffle-to-former bolt after the 15 operation years was calculated from dosimetry measurements in the head of the bolt and it was 1.2×10^{26} m^{-2} (E > 0.5 MeV), i.e., an equivalent neutron dose of 11.4 dpa **[36]**. However, the dose and also the dose rate decreasing gradient along the bolt length from the head towards the end of the shank is expected **[37]**. In this work, either retrospective dosimetry or any other experimental measurement was not performed to evaluate the dose gradient along the bolt. Nevertheless, the real dose along the bolt can be roughly estimated to ~7 dpa based on earlier works where the dose gradient was evaluated experimentally **[11, 12]**. In accordance to the referred data evaluating the dose attenuation by the material thickness, a rough estimation of the obtained dose in the end of the shank of the investigated bolt was.

The real operation temperature of the bolt is unknown. The temperature of the cooling water was lying in the range 269 – 298 ºC, but the true temperature of the component was higher due to the effect of gamma heating. Therefore, temperature in the bolt was calculated by 3D finite element modeling (FEM) with use of ABAQUS software **[38]** and it is shown in **Figure 3.1-1**. To evaluate the effects of the irradiation variable gradients, the TEM characterization was carried out in three positions along the bolt shank indicated in **Figure 3.1-1**.

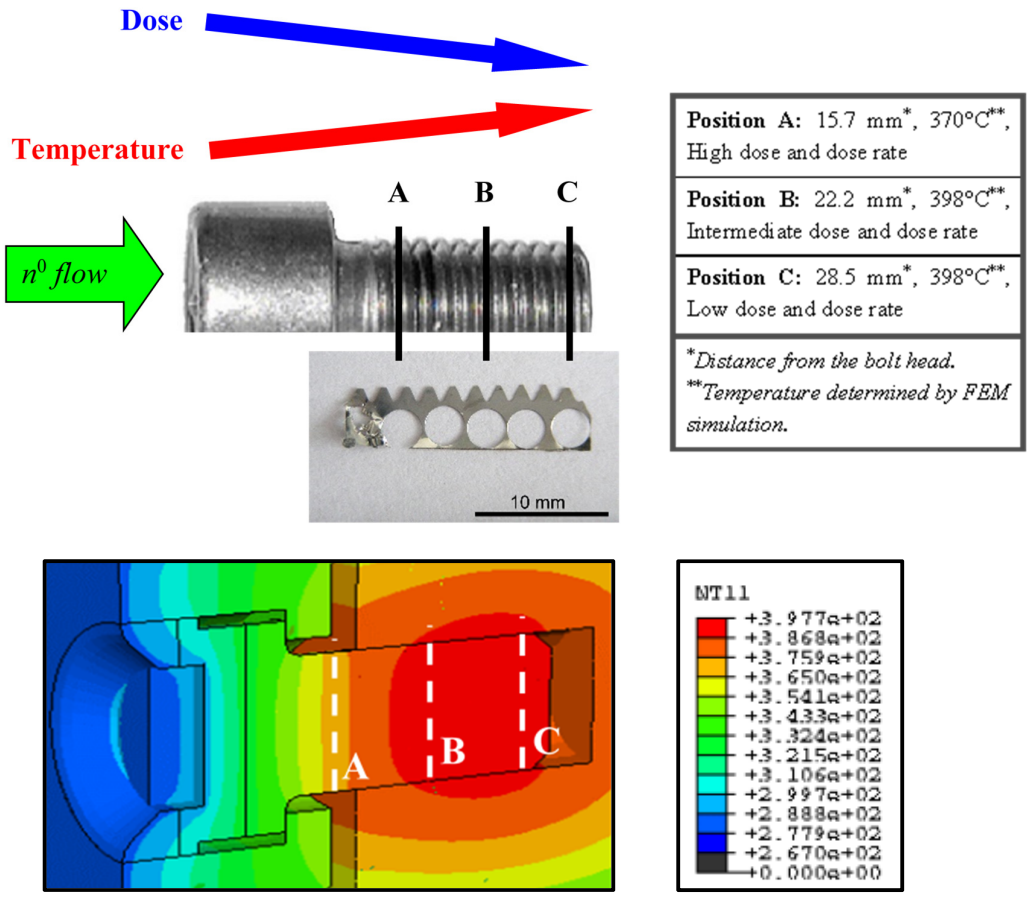

Figure 3.1-1: An outline of dose and temperature gradients along the bolt length. Positions A, B and C investigated by TEM and their distance measured from the bolt head are indicated. A FEM analysis below indicates the temperature gradient along the bolt due to the gamma heating **[38]**.

3.2 Results and discussion

3.2.1 Frank dislocation loops

Frank dislocation loops were the principal type of the radiation-induced damage microstructure determined along the Greifswald baffle-bolt. **Figure 3.2-1** depicts the TEM centered dark-field "rel-rod" images distinguishing single variants of edge-on Frank loops from the rest of the radiation microstructure. The "rel-rod" images were used for the loop measurements. Results of Frank loop average size, maximum size and density in Positions A, B and C are listed in **Table 3.2-1**, and the size distribution of Frank loops is given in **Figure 3.2-1**. The loop average size slightly decreases and the loop density slightly increases in the direction from bolt head, i.e. with increasing temperature and decreasing neutron dose and dose rate. However, these changes are very moderate and probably lying within the experimental

error. It indicates that Frank loops reached their steady state at all three positions and despite the temperature gradient. In fact, the temperature gradient should have an opposite effect on the loop development than it was ascertained via the loop size distributions. In each position, the size distribution has an asymmetrical shape with the main peak near 7 nm and broader tails exceeding about 25 nm. Based on the results, it can be concluded no significant effect of the irradiation gradients on the state of Frank loops in the Greifswald baffle-bolt. It is worth noting, that this finding is different with results from the Tihange PWR baffle bolt, which showed certain changes in Frank loop populations due to the irradiation gradients along the bolt with the maximum dose of 19.5 dpa in its head **[11]**.

Table 3.2-1: Results on Frank loops and cavities in the Greifswald baffle-bolt. Microhardness data are included **[13]**.

	Frank loops			**Cavities**			**Micro-hardness**
	Average size [nm]	Maximum size [nm]	Density [m^{-3}]	Average size [nm]	Maximum size [nm]	Density [m^{-3}]	MHV0.1
Position A	9.9	22.5	1.2E+22	2.0	7.2	5.8E+21	397.9
Position B	9.2	25.1	1.3E+22	3.5	9.7	4.6E+21	379.4
Position C	8.9	24.8	1.6E+22	6.9	15.5	2.3E+21	372.3

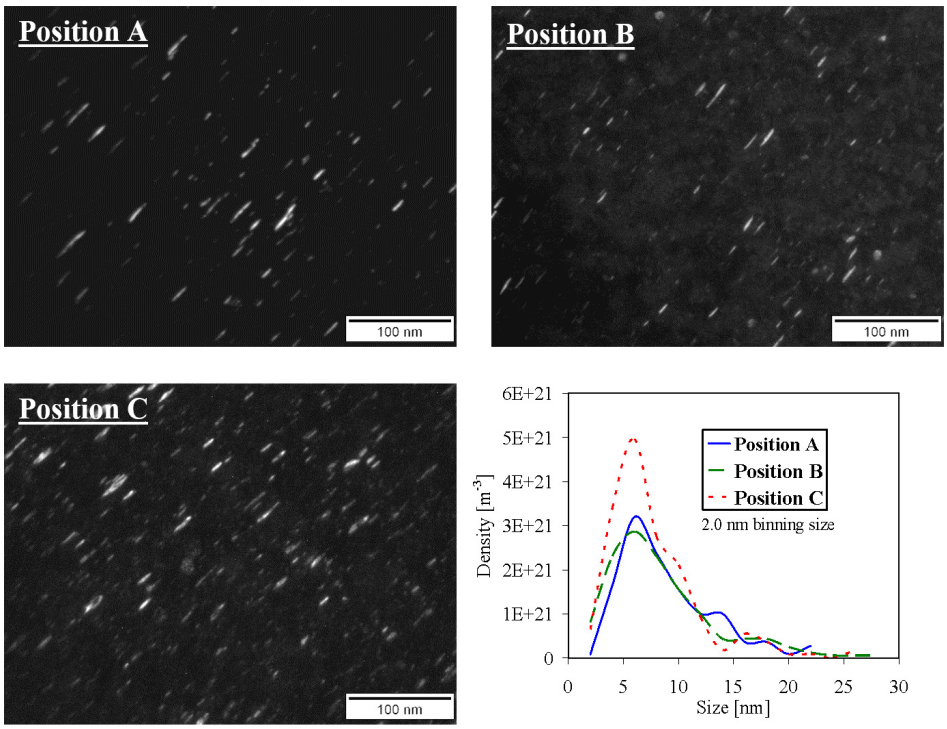

Figure 3.2-1: TEM-DF "rel-rod" images of one variant of edge-on Frank loops and plot of size distribution of Frank loops at each investigated position along the shank of the Greifswald baffle bolt.

3.2.2 Cavities

The characteristic micrographs of cavity populations in each position are shown in **Figure 3.2-2**. **Table 3.2-1** shows measured cavity average and maximum size and density in Positions A, B and C. The size distribution of cavities plotted in **Figure 5.1-4b** and all presented results show a wide difference in cavity population in the three investigated positions along the bolt shank.

In Position A, which was close to the reactor core and the cooling water and thus had the highest dose rate and the lowest irradiation temperature of the examined positions, cavities were observed predominantly with very fine size of 1-3 nm and some larger with size of 4-8 nm. This is documented by the cavity size distribution (**Figure 3.2-2**) with a dominant peak at 2 nm. Cavities in Position A had also the highest density. In Position B, the main narrow peak of the cavity size distribution also belongs to the range of 1-3 nm, however, a higher concentration of cavities with size of 4-10 nm shows their noticeable growth under the higher irradiation temperature, which was accompanied with a decrease of their density by factor of ~1.3. In Position C, the cavity size distribution revealed completely different results than in the foregoing positions. The measured cavity average size and density was circa two times larger and two times smaller, respectively, in comparison with Position B. The cavity size distribution revealed the narrow peak in the range of 1-3 nm too (even though its maximum position increased by ~0.5 nm), but its height was lower than another two wider peaks at 6 and 9 nm. The volumetric swelling (S) was calculated for each position using a relationship $S = \frac{\pi}{6} \cdot d^3 \cdot \rho \cdot 100$ from the known cavity average size d and cavity number density ρ. The swelling was 0.002 % in Position A, 0.010 % in Position B, and 0.040 % in Position C.

The effect of irradiation gradients along the Greifswald baffle bolt is obvious from the results. It can be assumed, that the irradiation temperature gradient in the range of circa 370 – 400 °C was the dominant factor affecting the cavity evolution, what agrees with results e.g. from the BN-350 irradiations revealing temperature as the dominant factor for cavity growth **[39]**. Additionally, a synergistic effect of the anticipated dose rate gradient along the bolt most likely influenced the cavity evolution at examined positions. The results agree with the expected enhanced cavity growth at lower dose rates, as it was determined in experimental irradiations **[40-43]** performed on several 300-type austenitic stainless steels (304, 316, 321) including their WWER equivalents.

The observed effects of irradiation variable gradients on the differences between the cavity microstructure in Positions A, B and C are in good agreement with the similar study of the Tihange PWR baffle bolt made of CW 316 SS **[11, 12]**. However, despite the temperature was ~50 °C lower in the Tihange bolt, the measured cavity average size, density and volumetric swelling were considerably lower in the Greifswald bolt (further documented *in the main document*, Figure 5.1-6). If the temperature effect on the cavity growth is considered as dominant above the dose differences **[39]**, this finding suggests that the used Ti-stabilized (and most likely cold-worked) 08Ch18N10T alloy for WWER baffle bolts is more resistant material

to volumetric swelling than the CW 316 SS counterpart in the PWR design. This is an interesting and important result that extends the previous experiments conducted on steels with different sink density but irradiated in a FBR and at higher temperatures of 400 – 500 °C **[3]**, where the better resistance of Ti-stabilized austenitic steels was also observed.

Although the measured level of swelling does not have to be of concern, it can be increased during the reactor lifetime and result in additional strain within the RVI component assembly and enhanced cavity formation on grain boundaries increasing the IASCC susceptibility (as studied and discussed in the second objective of this thesis).

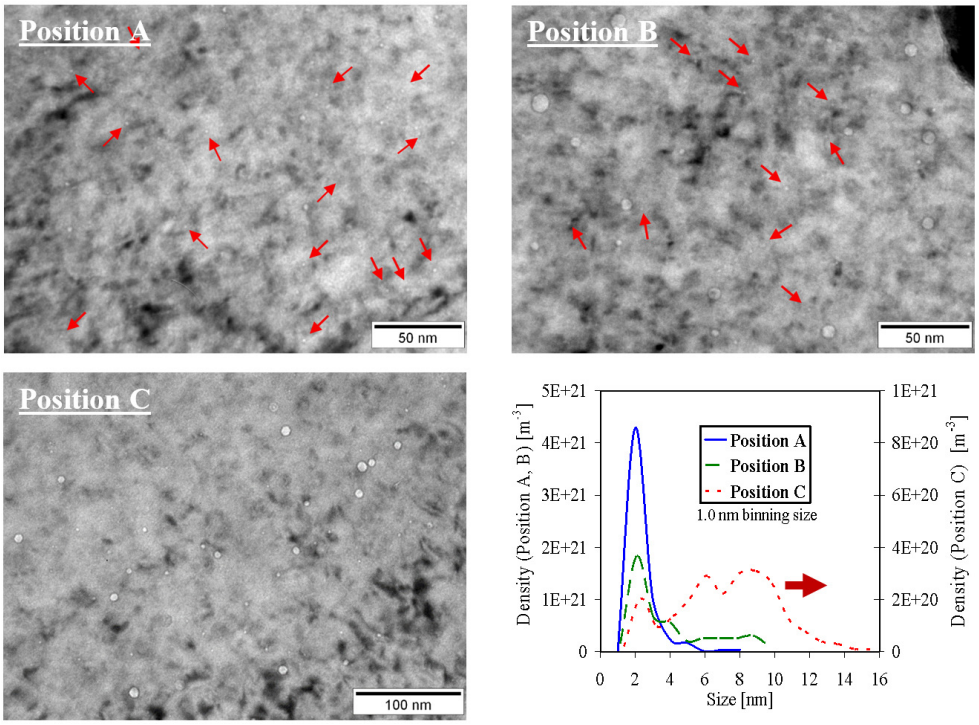

Figure 3.2-2: TEM-BF imaging of cavities at kinematical and underfocused conditions and plot of size distribution of cavities at each investigated position along the shank of the Greifswald baffle bolt. A distinct difference in cavity size distribution is apparent between the Positions A, B and C. Locations of the finest cavities are indicated with arrows. Note the scale differences in images.

3.2.3 Radiation-induced precipitates

The fine-scale RIP of secondary phases in the Greifswald baffle bolt was generally "lost" within the other radiation damage in TEM micrographs obtained under bright-field dynamical conditions. Therefore, it was necessary to use the centered TEM dark field imaging to distinguish them in the microstructure. No evidence of a diffraction motive representing γ' or G-phase precipitates was found, but the precipitates could be observed in the TEM-DF images using weak diffraction extra spots, **Figure 3.2-3**, unveiling the fine-scale precipitation,

most likely induced by the irradiation and present in each investigated position of the bolt. Please note, that at the time of the RIP investigation in the bolt, the methodology using extra spots had not been fully understood and could not be confirmed by the correlative STEM-EDX measurements. Thus, it was not easy to measure precipitates reliably and to declare unambiguous results. Nevertheless, it could be assumed from the observations, that there was an increasing tendency of radiation-induced precipitation in the Position B and C with higher irradiation temperature. The rough assessment of the RIP in Position C showed that their number density was in the order of 10^{22} m^{-3} and average size was ~4 nm, which is in good agreement with the results from other studies **[11, 17, 26, 44-47]**.

In this experiment, precipitates were studied with the use of extra spots present near austenitic zone axis [110] or $[\bar{1}14]$ tilted about 8° out of in-pole position for the first time. The diffraction patterns usually consisted from austenite reflections, weak "rel-rod" streaks from faulted Frank loops, and, extra spots tightly adjacent to the austenite reflections in groups of two or more dots and representing the fine precipitates. An example for both [110] and $[\bar{1}14]$ poles is shown in **Figures 3.2-3a,c**.

The above described observation of RIP can be related with presence of γ' phase with the FCC structure and the lattice parameter very similar with parameter of austenite, both has $a_0 \approx 0.36$ nm. The similar crystallography of both phases may cause the existence of precipitate spots close to the matrix reflections. The observation of RIP with the use of weak extra spots lying in the vicinity of the matrix reflections in the tilted [110] zone axis was carried out in another study of SA 304 SS irradiated to 24 dpa at 300°C in Chooz A PWR reactor **[48]**, where the present RIP also did not show a clear diffraction motive. The subsequent APT measurements determined formation of the Ni_3Si γ' precipitates **[49]**. The relationship of the extra spots with the γ' phase further described in *the main document* and confirmed in the third objective of this thesis via the STEM-EDX mapping.

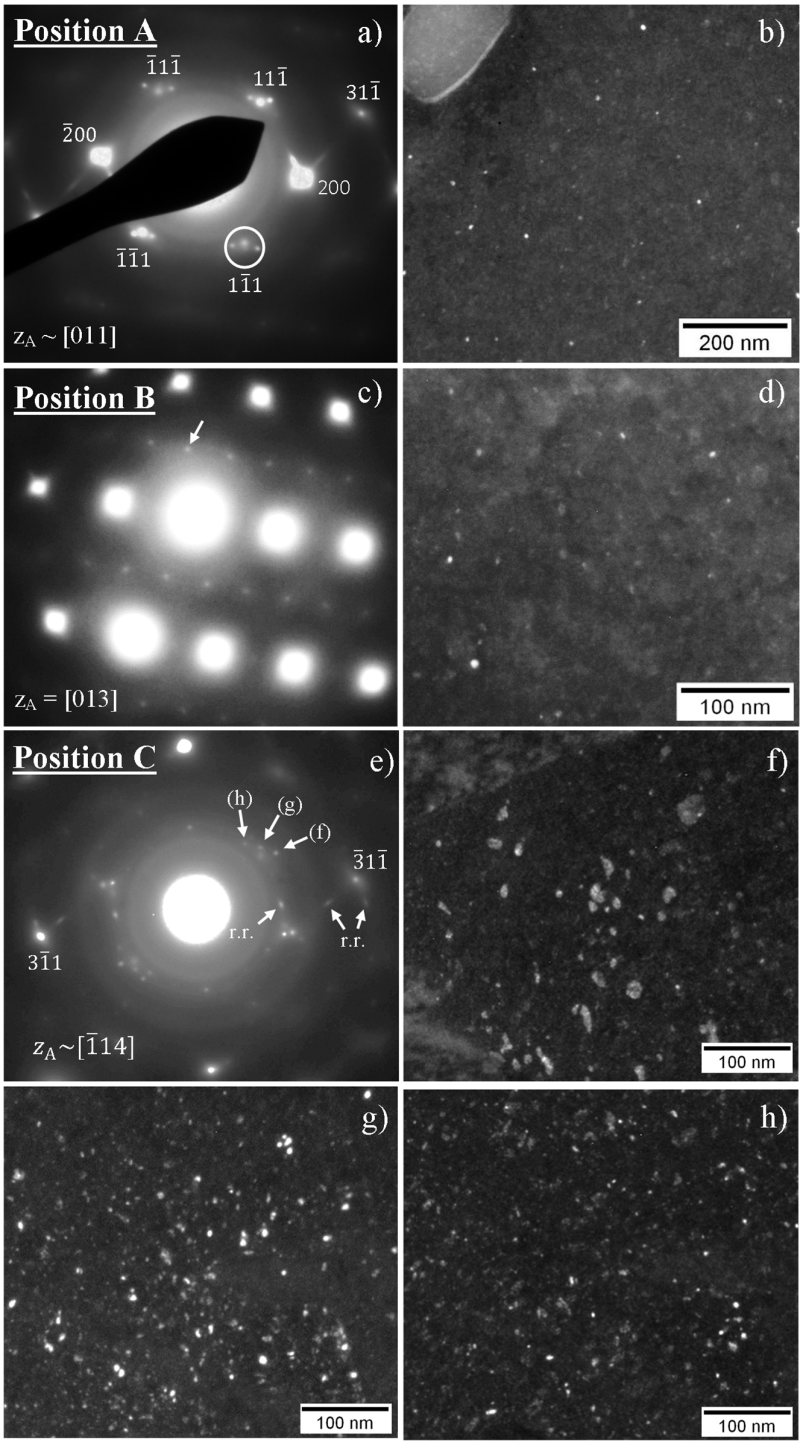

Figure 3.2-3: RIP in Greifswald baffle bolt. Position A: SAED of the matrix close to zone axis [011] with indicated extra spots selected by a larger aperture (a). Corresponding TEM-DF image of fine precipitates (b). Position B: SAED of the matrix at zone axis [013] containing forbidden reflections (indicated by arrow) (c). TEM-DF image of RIP with use of the indicated reflection (d). Position C, SAED of the matrix close to zone axis $[\bar{1}14]$ and centered TEM-DF investigation of three indicated extra spots (e) resulting in images of planarly oriented Frank loops (f) and fine RIP (g, h). Images (f-h) are acquired from the same place. "r.r." indicates "rel-rod" streaks from inclined Frank loops.

4 Baffle bolt irradiated in an experimental reactor

4.1 Experimental

The investigated material was a CW 316 SS irradiated at temperature of 300 °C in form of slow-strain rate test (SSRT) samples in the SM high-flux research light-water reactor at RIAR, Russia. To study the effect of helium content on the IASCC susceptibility, the samples were irradiated in two positions with fast and thermalized (mixed) neutron spectra simulating irradiation in a FBR and in a PWR reactor, respectively. The corrosion tests were conducted in ÚJV autoclave with high temperature loop **[21]** and they were followed by the TEM at the same site.

The chemical composition of the alloy is given in **Table 4.1-1**. The particular heat of the material was 15% cold worked, with fully austenitic microstructure. The cold-worked microstructure consisted of numerous deformations twins within polygonal grains (30-40 μm in size) and a dense dislocation network organized in cells within the grain matrix **[19]**.

Table 4.1-1: Chemical composition of the EDF CW 316 SS, in wt. % (B, O and P in ppm) **[21]**.

C	S	P	Si	Mn	Ni	Cr	Mo	Cu	Co	Nb	Ti	B	O	N
0.054	0.022	0.027	0.68	1.12	10.6	16.6	2.25	0.24	0.12	0.01	<0.01	5	41	230

The different He production rates via transmutations were achieved by two irradiation conditions:

1. In a position shielded by ^{77}Hf against thermal neutrons and with predominantly fast neutron flux emulating the FBR environment (samples assigned “B58”). The shielding is depicted in **Figure 4.1-1**.
2. In a position without shielding with both thermal and fast neutron fluxes emulating the PWR environment (samples assigned “B56”).

The calculated He production rate was about 2 – 3 appm/dpa in the fast spectrum and between 40 and 70 appm/dpa in the mixed spectrum **[19]**. Excepting the differences in the neutron spectra and He production rates, other irradiation variables were considered to be equivalent between both positions (i.e., temperature, dose rate, final dose). The dose rate was approximately ~2.5–3×10^{-7} dpa/s and the accumulated dose in B56 and B58 samples was 15 dpa and 16 dpa, respectively. Later on, the irradiation dose of 15 dpa is referred for both samples. The helium production comes from nuclear reactions mainly with nickel. The helium production rate was calculated by RIAR assuming that the ^{58}Ni (n, γ)^{59}Ni reaction followed by

^{59}Ni (n, α)^{56}Fe reaction is the main helium production source. Because those reactions are involved mainly by thermal neutrons,

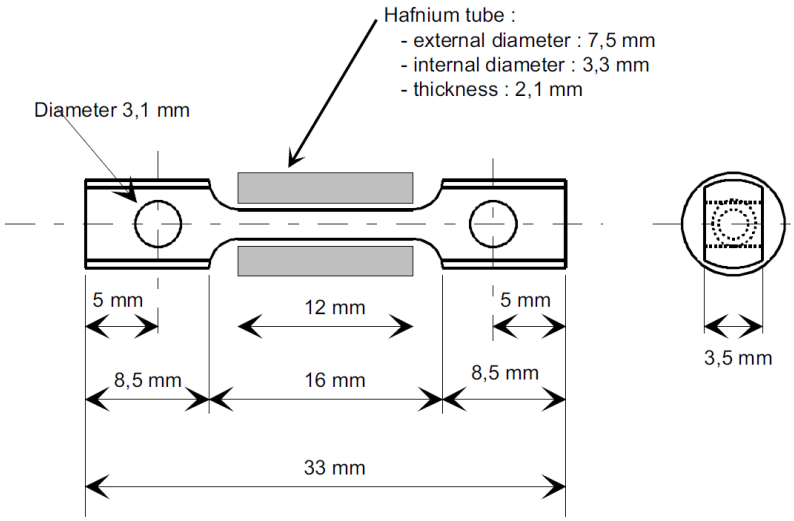

Figure 4.1-1: Tensile specimen for SSRT test with Hf shielding **[19, 21]** .

4.2 Results

4.2.1 Frank dislocation loops

The microstructure of specimens B56 and B58 consisted from initial cold-worked microstructure in form of numerous deformation twins, deformation bands and probably transformation phases (e.g. α-martensite) in cross-sections of twins and bands.

Frank loops were the principal component of the radiation damaged microstructure. They were imaged in the edge-on orientation under the centered TEM-DF "rel-rod" conditions near the [011] matrix zone axis. Examples of edge-on Frank loops in specimens B56 and B58 are shown in **Figure 4.2-1**. The average size and the number density of Frank loops evaluated from specimens B56 and B58 are given in the **Table 4.2-1**. The size distribution of Frank loops is presented in **Figure 4.2-1**. Regardless the spectrum type, both size distributions are nearly identical. They are asymmetrical in shape with a main peak around 10 nm and wide tails extending up to 30 – 40 nm in size for all specimens. At the same time, the measured average size and the number density of loops are nearly identical and they do not change above an experimental error between the four conditions. It gives an evidence that the saturation of Frank loops development occurred at a lower neutron dose and that there was not any apparent influence of different neutron spectra on the Frank loop evolution.

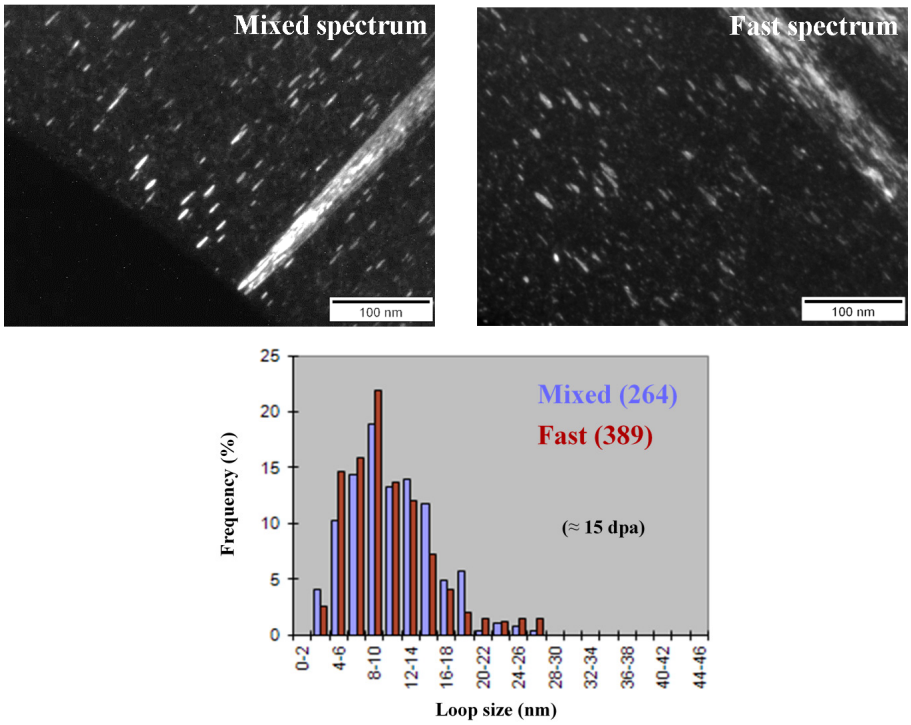

Figure 4.2-1: TEM-DF "rel-rod" images of one variant of edge-on Frank loops and plot of size distribution of Frank loops in the CW 316 SS after irradiation in mixed and fast neutron spectrum (a number of measured loops is given in brackets). Twins oriented on the same {111} planes as loops are present in images.

Table 4.2-1: Results on Frank dislocation loops and cavities in the CW 316 SS irradiated at 300°C with neutrons of mixed and fast spectra.

Specimen	Irradiation condition		Frank Loops		Cavities	
	Neutron spectra	**Dose** (dpa)	ρ ($\times 10^{22}$ m^{-3})	***d*** (nm)	N_V ($\times 10^{22}$ m^{-3})	***d**** (nm)
B 56	Mixed	15.0	2.6	10.4±4.6	7.7 ± 1.7	1–4
B 58	Fast	16.1	2.3	10.9±4.7	1.4 ± 0.8	0.7–3

ρ = number density, **d** = average size, **d*** = size range

4.2.2 Cavities

The most significant microstructure observation in this study was the ascertained difference in cavity populations present in specimens B56 and B58. The irradiation in SM reactor with mixed spectrum, with more than twenty times higher helium production rate than the SM fast spectrum, resulted in higher cavity density by factor of ~5.5 in B56 specimens than

in B58 specimens irradiated with the fast spectrum. In all the samples examined, only very fine nanocavities were found. Cavities mostly between 1 and 2 nm in size, and some of them 3-4 nm at maximum, were found in the specimen B56. However, in the specimen B58, cavities were found with a maximum size of 1 nm, and many of them were around 0.7 nm in size. TEM micrographs in **Figures 4.2-2** document presence of cavities in both specimens B56 and B58 irradiated to 15 dpa. Evaluated data of cavity number density and cavity size range are given in the **Table 4.2-1**. In the specimen B56 with higher cavity density, cavities are distributed homogenously within grains matrix, however, some cavities are clustered and some are more separated from the others. In the specimen B58 with lower cavity density, cavities are distributed rather randomly. It was not possible to distinguish nature of cavities (i.e., vacancy voids and helium bubbles) with the available conventional TEM device and because of the very small cavity size.

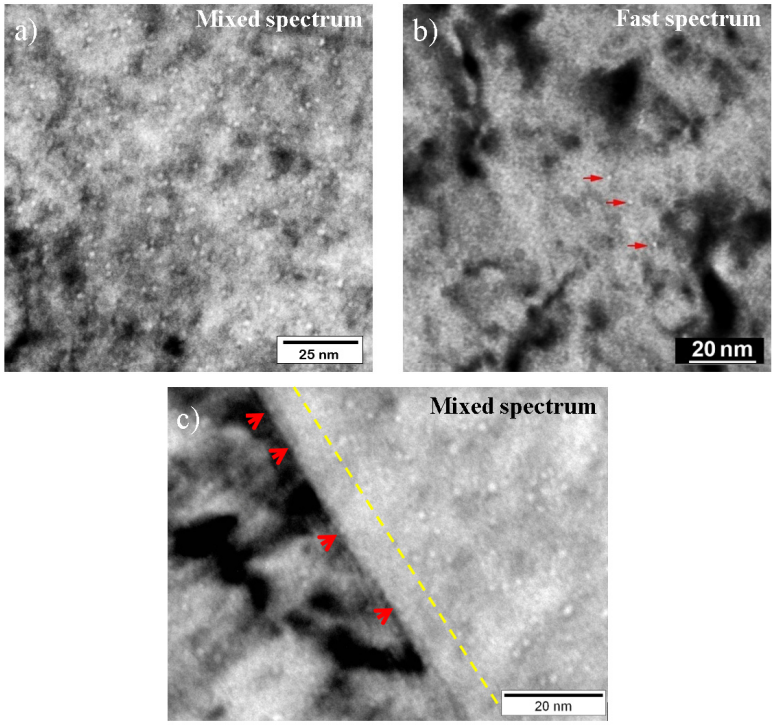

Figure 4.2-2: Cavities of high density in specimen B56, mixed spectrum (a). Cavities of low density (marked by red arrows) in specimen B58, fast spectrum (b). Cavity denuded zone (marked by yellow dashed line) along a GB. GB is decorated by solitary cavities (marked by red arrows), specimen B56 (c). All images are taken under TEM kinematical underfocused conditions.

The examination of cavities was performed also along edge-on high-angle grain boundaries where is a concern of potential influence of radiation damage denuded zones increasing IASCC susceptibility. The Frank loop density dilution along the boundaries was not observed, but, the TEM image taken at higher magnification in **Figure 4.2-2c** shows a cavity denuded zone in the specimen B56 irradiated with the mixed spectrum. The denuded zones

were about 10-15 nm in width and the cavity dilution was accompanied by solitary cavities indicated directly at the grain boundary. These cavities were found with smaller size than their counterparts in the matrix and their linear spacing on the boundary was circa 10-20 nm. In the case of the specimen B58, the grain boundary cavity enhancement cannot be excluded, but there was no evidence of any preferential cavity formation along grain boundaries due to the very low cavity density.

4.2.3 Radiation-induced precipitates

Fine-scale RIP of a secondary phase was observed homogeneously distributed in the matrix of both specimens B56 and B58. They were revealed by the centered TEM-DF images with use of extra spots. The extra spots suitable for the RIP observation were found near austenitic zone axes [110] or [114] tilted out about 8° into the same conditions as for the "rel-rod" imaging of Frank loops. Such diffraction patterns usually contain weak matrix reflections, the streaks and spots from edge-on and planar Frank loops, and from extra spots representing RIP. The same approach was used for the RIP observation in the previous objective and it is described in detail in the main document of this thesis.

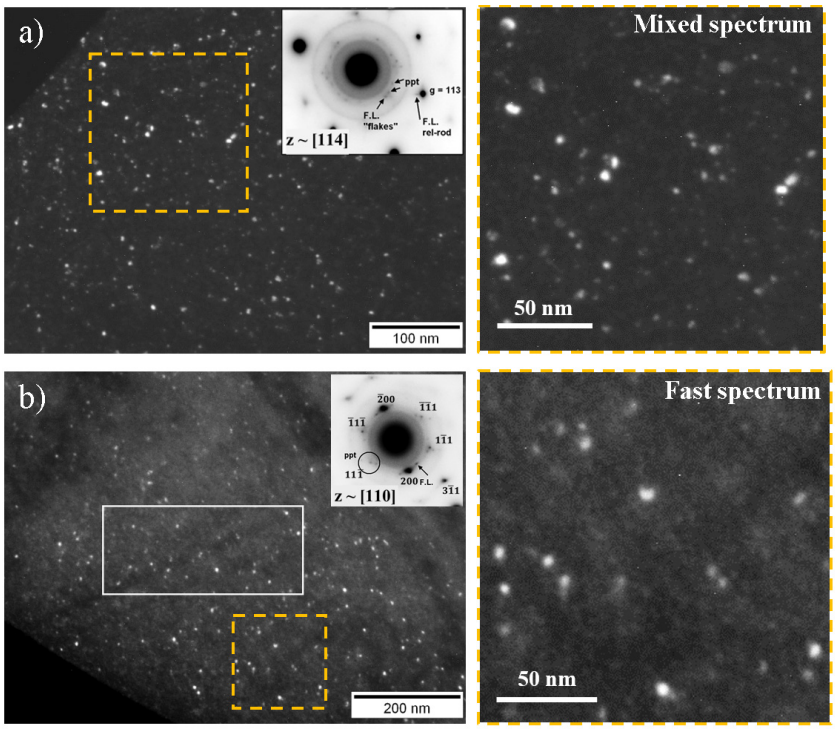

Figure 4.2-3: TEM-DF images of RIP in the specimen B56, mixed spectrum (a) and in the specimen B58, fast spectrum (b). The used extra spots for the imaging are marked as "ppt" in the inserted SAED patterns. The enlarged areas of original images are marked by orange dashed squares.

TEM-DF images of RIP in specimens irradiated by mixed and fast neutron spectra are represented in **Figure 4.2-3**. For both specimens the size of observed RIP was in the range of 1 – 7 nm. The measured average size and number density of RIP was 2.7 nm and 1.74×10^{22} m^{-3} in specimen B56 and 3.3 nm and 0.68×10^{22} m^{-3} in specimen B58. The differences in RIP measurements between two conditions could be influenced by sample quality, since only very thin areas of TEM foils were suitable for observation of RIP and B58 sample was evaluated from thicker foil hiding the smallest precipitates. In addition, the real RIP density in both specimens can be higher, since each extra diffraction spot may represent only a part of the RIP population.

4.3 Discussion

The SSRT tests conducted on CW 316 SS in PWR primary water showed an influence of neutron spectrum after the dose of 15 dpa **[21]**. The tests of mixed spectrum specimens revealed remarkable decrease in ductility of the specimen B56 compared to the specimen B58 (total elongation of 1.4 % vs. 7.7 %). The subsequent SEM fractography revealed high amount of defective intergranular cracking in this specimen compared to the specimen B58 (IG ≈ 37 % vs. IG ≈ 0%). This indicates the IASCC mechanism of the cracking.

The microstructure of specimens B56 and B58 after the SM irradiation at 300°C was heavily damaged radiation-induced defects of high density in form of Frank loops, cavities and radiation-induced precipitates. In addition, hardly discernible fine defects of "black-dot" type were observed too. This qualitative assessment overall agrees with other observations of neutron irradiated CW 316 SSs at temperatures around 300 °C **[2]**.

Frank dislocation loops were primary type of damage in both specimens with the main contribution to the radiation hardening of the material. As it was discussed e.g. in **[50]**, the irradiation hardening has a strong correlation with the IASCC sensitization. However, the observed Frank loops in both specimens irradiated in mixed and fast spectra were found without any important difference. Therefore, another microstructural factor leading to the different IASCC susceptibility of the material should exist.

Radiation-induced precipitates have been found in both specimens B56 and B58. The population of precipitates most probably consists of nickel-silicon-rich phase of γ′. Because they are expected in coherent or semi-coherent relationship with the austenitic matrix, they participate on the material irradiation hardening by a matrix dispersive strengthening **[51]**. Since there has been found similar distribution of these precipitates in both specimens, only a minor or rather no effect of the precipitation to the different fracture behavior can be assumed.

The only observed significant difference in the radiation damage microstructure was in the cavity population between the irradiated specimens with different spectra. Cavities were found very fine (1 nm and below) in the fast spectrum specimen and larger (1-4 nm) in the mixed spectrum specimen, but the number density in the mixed spectrum specimen was higher

by factor of ~5.7 than in the fast spectrum specimen. This observation corresponds with the different helium production rates under each SM irradiation condition, were the mixed spectrum could produce helium up to 35-times faster. In comparison with literature data, the cavity density and size range measured in mixed spectrum specimen B56 is very close to the results from the CW 316 SS FTT irradiated in PWR spectrum at 290°C to 33 dpa **[52]**.

Cavities are not considered to contribute to the yield strength increment and the irradiation hardening of the austenitic steels irradiated at PWR relevant temperatures below 400 °C, where they are considerably small and behave rather as soft obstacles for the moving dislocations **[53-56]**. However, He-induced embrittlement can be severe, if enough He bubbles form at grain boundaries and induce intergranular failure **[53]**.

The TEM of grain boundary microstructure of the specimen B56 with higher He content and cavity density revealed cavity denuded zones about 10-15 nm in width along a high-angle grain boundary accompanied by solitary cavities indicated directly at the grain boundary. The occurrence of the denuded zones was investigated also in the PWR irradiated CW 316 SS FTT **[56]**, where the cavity denuded zones of the same width and also the enhanced cavity formation at grain boundaries were observed. These observations of the cavity microstructure along and at grain boundaries suggests that cavities are somehow enhanced at the grain boundary at the expense of the adjacent matrix. This can be attributed to several possible synergistic mechanisms:

1) Flux of vacancies caused by radiation-induced segregation of solute elements towards and away the grain boundary **[2]** may result in increase of vacancy density at the boundary and decrease of vacancy density in matrix adjacent to the boundary.

2) He generated in the microstructure from transmutations enhances nucleation and growth of cavities (in form of voids and/or He-bubbles) **[22]**, thus the density of cavities can be logically enhanced in areas with higher vacancy concentration, i.e., at the boundaries, and suppressed within the adjacent vacancy denuded zone. It was not possible to distinguish the nature of cavities in this study, but presence of both He-bubbles and vacancy voids in the irradiated microstructure of the mixed spectrum specimen B56 can be expected. In accordance to He stabilization effect on cavities **[22]**, the higher cavity density in this sample was, firstly, due to the higher He production rate producing higher number of He-bubbles, and, secondly, due to enhanced nucleation rate and stability of vacancy voids stabilized by higher He content within the matrix.

3) The RIS substantially increases Ni concentration at grain boundaries of austenitic steels **[2]**. At the PWR relevant irradiation conditions, the RIS of Ni reaches a steady state at a dose of ~5-10 dpa, when Ni concentration can increase more than 15 at. % above the matrix concentration at high-angle grain boundaries (see Figure 2.4-15 in the *main document*). In addition, it has been often observed (e.g., in **[16, 17]** and in RIS results from self-ion irradiations presented in this work and in **[32]**) Ni depletion below the Ni matrix concentration by ~3 at. % within the RIS affected zone along the boundaries with a width of 10-5 nm (which is the same width as of the observed cavity dilution zone). Hence, the created RIS profile of Ni

concentration may result in variation of the He and H production rate across the grain boundary and enhance the preferential cavity formation at the boundary site. A supplementary contribution to the effect of high Ni concentrations at grain boundaries may have boron, which can be thermally segregated at boundaries and transmuted to He **[58]**.

Considering the complex interplay of synergistic effect of the potential mechanisms influencing the cavity formation at grain boundaries, this mode of degradation may be of high importance when the radiation-induced damage microstructure is put in context with the differences observed in fracture behavior and IASCC susceptibility between the irradiated specimens in the mixed and fast neutron spectra.

5 Baffle bolt irradiated by self-ions in an accelerator

5.1 Experimental

The material meeting the criteria established in the introduction part is CW 316 SS) designed for PWR baffle-bolts and manufactured in France. The material was irradiated in a Russian BOR-60 FBR to doses 5.5, 10, 15, 25 and 46 dpa at irradiation temperature of 320°C and with a dose rate of $5x10^{-7}$ dpa/s. The alloy was characterized within the CIR Program **[16, 17, 59]**, where it was designated as Heat B. Archive material was available from Pacific Northwest National Laboratory. The chemical bulk composition of the material is given in **Table 5.1-1**. The characteristics of non-irradiated microstructure of the CW 316 SS Heat B is available throughout literature **[16, 17, 20, 59]**. The level of cold-work was 20 % and it produced heavily deformed microstructure with a large amount of deformation twins and micro-twins and a dense dislocation network. The extensive deformation led to highly twisted grain boundaries with frequent intersections with twins. The grain structure was equiaxed with grain size 15-30 μm. In the non-irradiated state, grain boundaries were slightly enriched by Cr, but relatively strongly enriched by Mo and P **[53]**.

Table 5.1-1: Bulk chemical composition (wt. %) of the studied baffle-bolt CW 316 SS Heat B **[16]**.

C	Mn	Si	P	S	Cr	Ni	Mo	N	Ti	Co	Cu	Fe
0.056	1.13	0.73	0.022	0.022	16.84	10.54	2.25	0.021	0.01	0.056	0.25	68.07

Samples for the self-ion irradiations were prepared from the bulk material by electric-discharge machining in the form of 20 mm × 3 mm × 1.5 mm TEM bars, **Figure 5.1-1a**. The surface selected for irradiation was mechanically polished up to #4000 grit SiC paper followed by 30-60 second electropolishing in a 90% methanol, 10% perchloric acid solution at -40ºC to produce a mirror-like surface without a mechanically induced damage layer.

The irradiations were conducted with 5 MeV Ni^{++} or Fe^{++} ions in a 1.7 MV General Ionex Tandem Accelerator at Michigan Ion Beam Laboratory. A specially designed copper heating stage and temperature monitoring using Stinger thermal imaging camera system. The thermal imager provided real-time temperature measurements throughout the irradiation. The temperature variation was kept within 10 °C of the target temperature. Details about the stage set-up can be found in **[60]** and details about the accelerator instrumentation and operation, including temperature monitoring and control, ion beam control, ion beam current measurement or ion dose calculation, can be found in **[61]**.

The Stopping and Range of Ions in Matter Monte-Carlo simulation software SRIM-2008 **[62]** was used to calculate damage rate and penetration depth of 5 MeV Ni^{++} and Fe^{++} ions, **Figure 5.1-1c**. A displacement energy was selected 40 eV for the major alloy elements with respect to an ASTM standard **[63].** The first irradiations were conducted with Ni^{++} ions and they were substituted later by Fe^{++} ions to minimize a potential effect of radiation damage enhancement by implanted Ni self-interstitials, because Ni (as the main alloying element) participates strongly on RIS.

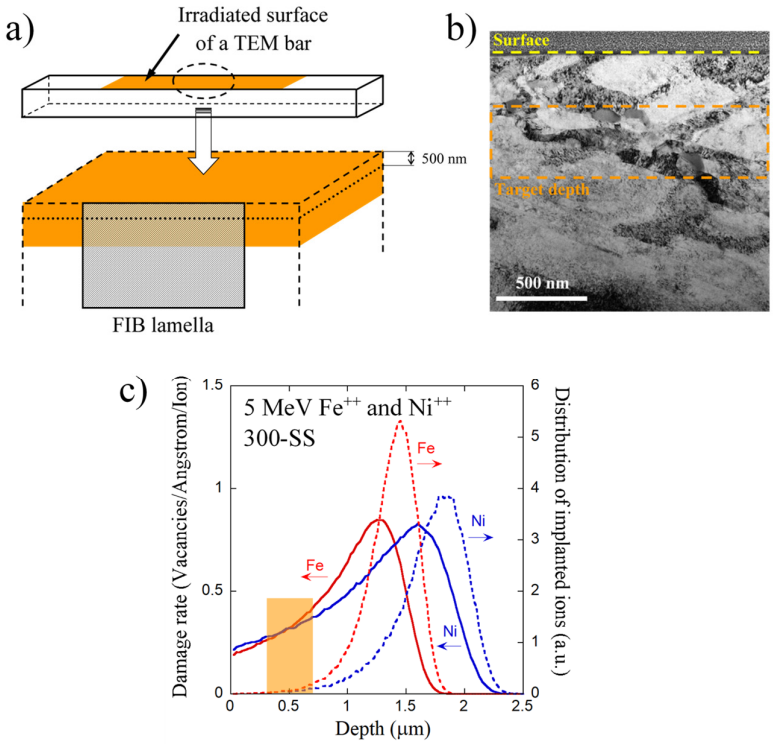

Figure 5.1-1: A drawing of TEM bar and FIB cross-sectional lamella from the ion irradiated surface (a). A TEM image of the FIB lamella with indicated target depth interval for TEM characterization (b). A SRIM simulation of damage rate and ion implantation depth of self-ions in a 300-grade stainless steel, the target depth interval is indicated by orange rectangle (c).

Table 5.1-2: Temperatures and doses used for the self-ion irradiations of CW 316 SS Heat B.

Irradiation temperature	Irradiation dose	Used ions
380 °C	23 dpa	5 MeV Fe^{++}
380 °C	130 dpa	5 MeV Ni^{++}
500 °C	23 dpa	5 MeV Ni^{++}
600 °C	15 dpa	5 MeV Fe^{++}

The neutron dose rate during the BOR-60 irradiation was ~$5x10^{-7}$ dpa/s and the irradiation temperature was 320 °C. However, for Ni^{++} or Fe^{++} irradiations, the dose rate was ~$1x10^{-3}$ dpa/s. Two self-ion irradiation temperature shifts compensating the dose rate difference were established by the Mansur's equations introduced and plotted in the *main document* (equations (4) and (5), Figure 4.3-5) to preserve microstructure and RIS, respectively. As a result, the self-ion irradiation temperature to match microstructure was 362 °C and the self-ion irradiation temperature to match RIS was 601 °C. Proton irradiation at a dose rate of ~10^{-5} dpa/s has been used extensively **[64, 65]** to simulate neutron irradiation microstructure with a temperature shift of ~40 °C. Self- ion irradiations with higher dose rates are expected to have larger temperature shifts. Therefore, the irradiation temperature to match microstructure was selected to be 380 °C, about 20 °C higher than was calculated. The established self-ion irradiation conditions for the presented experiments are listed in **Table 5.1-2**.

5.2 Results and discussion

5.2.1 Frank loops

The state of the dislocation microstructure in the self-ion irradiated CW 316 SS Heat B depended on the irradiation temperature and it is documented in **Figures 5.2-2**.

At 380 °C, the original dense dislocation network produced by the cold work was substituted by a dense population of Frank dislocation loops. However, short dislocation segments were still present after the dose of 23 dpa. After 130 dpa, the segments have not been observed unambiguously. TEM-DF "rel-rod" images unveiling presence of edge-on Frank loops at one of four sets of (111) austenitic lattice planes are presented from each irradiation condition in **Figures 5.2-2**. Results of Frank loop average size and number density are listed in **Table 5.2-1**, and Frank loop size distributions for all irradiation conditions are shown in **Figure 5.2-3**. All these results demonstrate that Frank loops in CW 316 SS Heat B varied considerably between irradiation temperatures.

At 380 °C, the irradiations to 23 dpa and 130 dpa produced Frank loops with size range of 1.3-40.1 nm and 0.8-36.9 nm, average size of 8.8 nm and 7.7 nm, and number density of 3.8 × 10^{22} m^{-3} and 6.2 ×10^{22} m^{-3}, respectively. The smaller average size and the nearly doubled density after 130 dpa suggests some degree of continuous evolution of the Frank loop population between the two doses. The loop size distributions for both doses are asymmetrical at this temperature, but each with certain differences. For 23 dpa, it has a narrow peak with a maximum at ~4.0 nm and a broader tail extending up to ~30 nm. For 130 dpa, it has sharper peak with maximum ~2.5 nm and a small secondary peak at ~20 nm in the extending tail. That suggests the Frank loop density was increasing by nucleation of new loops with the smallest size while a part of larger loops was growing with the increasing dose. Even though the

observed differences are not substantial between two doses, this finding may indicate that Frank loops did not reached a steady-state in the earlier doses below 10 dpa as expected [2], but a moderate loop evolution continued after 23 dpa.

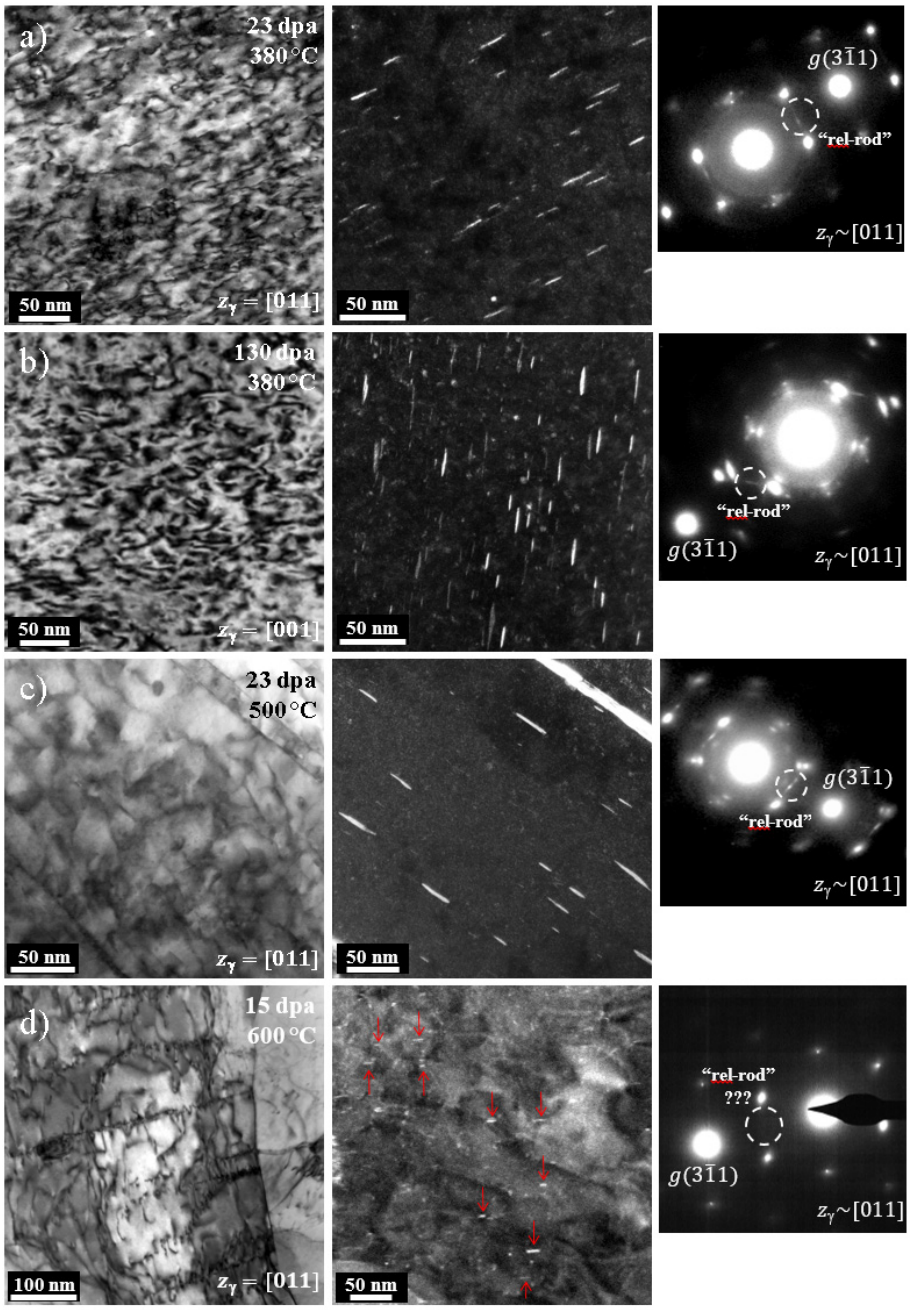

Figure 5.2-2: (S)TEM-BF down-zone images of the dislocation network and TEM dark-field "rel-rod" images of edge-on Frank loops with corresponding SAED patterns after 5 MeV self-ion irradiations to 23 dpa at 380 °C(a), 130 dpa at 380°C(b), 23 dpa at 500 °C (c) and 15 dpa at 600 °C(d).

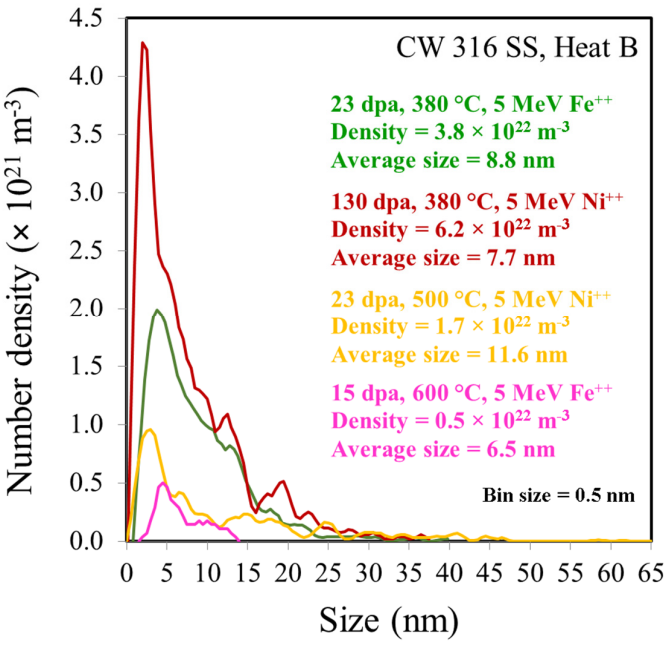

Figure 5.2-3: Size distributions of Frank dislocation loops in the CW 316 SS Heat B irradiated by 5 MeV self-ions at different temperatures and doses.

At 500 °C, the original dislocation network was replaced by dislocation loops partially after the dose of 23 dpa, and the dislocation segments were present apparently in larger amount than at 380 °C. The Frank loop population was with size range of 0.9-62.5 nm, average size of 11.6 nm and a low density of 1.7×10^{22} m^{-3}. The observed coarsening of Frank loops with size frequently larger than 40 nm and the substantial decrease in loop density in comparison with 380 °C indicates an increased mobility of radiation-induced point defects.

At 600 °C, the original dislocation network appeared retained after the dose of 15 dpa. The presence of Frank loops is not generally expected due to a high point-defect mobility to sinks at this temperature regime. The rapid decrease of Frank loop density at irradiation temperatures above 400 °C documents Figure 2.4-8 in the *main document*, which forecasts very low Frank loop density of ~10^{19} m^{-3} in neutron-irradiated austenitic stainless steels at ~600 °C **[66]**. The SAED and TEM-DF imaging under proper TEM-DF "rel-rod" conditions was performed to verify this assumption. No "rel-rod" streaks appeared in the SAED pattern, however, if the objective aperture was placed at the assumed streak position (**Figure 5.2-2d**), surprisingly, the resulting TEM-DF imaging revealed small edge-on Frank loops with a roughly estimated size range of 3.3-13 nm, average size of ~6.5 nm and a low number density of ~0.5 × 10^{22} m^{-3} after the 600 °C irradiation to 15 dpa.

Aside from the Frank dislocation loop microstructure, any stacking fault tetrahedra (SFT) were not observed at any condition of self-ion irradiations.

Table 5.2-1: Results of Frank dislocation loops, RIP, and RIS at HAGB in CW 316 SS Heat B after BOR-60 **[16, 17]** and 5 MeV self-ion irradiations.

Dose, Temperature, Particles	Dose rate (dpa/s)	Frank dislocation loops		RIP (TEM-DF) *RIP (STEM-EDX)*		Cavities
		Avg. Size (nm)	Density ($\times 10^{22}$ m^{-3})	Avg. Size (nm)	Density ($\times 10^{22}$ m^{-3})	
25 dpa, 320 °C, Fast neutrons	5×10^{-7}	7.8	14	5.7 *N/A*	1 *N/A*	not present
46 dpa, 320 °C, Fast neutrons	5×10^{-7}	6.2	23	5 *N/A*	1 *N/A*	not present
23 dpa, 380 °C, 5 MeV Fe^{++}	10^{-3}	8.8	3.8	5.2 *8.9*	1.8 *5.7*	not present
130 dpa, 380 °C, 5 MeV Ni^{++}	10^{-3}	7.7	6.2	4.1 *7.9*	1.8 *4.3*	not present
23 dpa, 500 °C, 5 MeV Ni^{++}	10^{-3}	11.6	1.7	N/A *6.6*	N/A *0.3*	not present
15 dpa, 600 °C, 5 MeV Fe^{++}	10^{-3}	6.5	0.5	N/A *13.6*	N/A *0.03*	not present

Dose, Temperature, Particles		Si	P	Cr	Mn	Fe	Ni	Mo
		(wt. %)						
25 dpa, 320 °C, Fast neutrons	HAGB composition	2.7	0.4	13.9	N/A	N/A	18.2	1.2
	Difference from matrix	2.0	0.4	-2.9	N/A	N/A	7.7	-1.1
46 dpa, 320 °C, Fast neutrons	HAGB composition	2.4	0.3	13.0	N/A	N/A	18.6	0.7
	Difference from matrix	1.7	0.3	-3.8	N/A	N/A	8.1	-1.6
23 dpa, 380 °C, 5 MeV Fe^{++}	HAGB composition	3.5	0.4	11.8	0.7	58.0	23.6	1.4
	Difference from matrix	2.7	0.4	-5.2	-0.5	-9.9	12.8	-0.8
130 dpa, 380 °C, 5 MeV Ni^{++}	HAGB composition	3.0	0.3	12.3	0.6	59.6	22.2	1.6
	Difference from matrix	2.3	0.3	-4.9	-0.6	-8.0	11.3	-0.9
23 dpa, 500 °C, 5 MeV Ni^{++}	HAGB composition	4.0	0.1	10.9	0.5	58.6	23.9	1.0
	Difference from matrix	3.2	0.1	-6.1	-0.7	-9.3	12.9	-1.2
15 dpa, 600 °C, 5 MeV Fe^{++}	HAGB composition	1.3	0.1	12.4	0.5	65.2	18.1	N/A
	Difference from matrix	0.5	0.1	-4.7	-0.6	-2.4	7.1	N/A

5.2.2 Cavities

The presence of voids was inspected in the self-ion irradiated CW 316 SS Heat B material irradiated at all temperatures with use of the through-focal technique. Nevertheless, no evidence of voids was found within the target irradiation depth at any irradiation dose and temperature. However, larger voids with size reaching 25 nm were found after the irradiation at 500 °C but in the region affected by sample the surface (i.e., away from the target depth).

5.2.3 Radiation-induced segregation

The RIS was measured only at high-energy high-angle grain boundaries (HAGB). To obtain representative dataset, at least two different HAGBs were measured at each condition and each measured boundary was analyzed at several positions within the target irradiation depth. Results in form of average grain boundary chemical composition and the composition difference between the boundary and the austenitic matrix are listed in **Table 5.2-1**.

The measurements revealed HAGBs enriched or depleted by solutes with the same trend typical for CW 316 SSs irradiated by neutrons. However, the intensity of the RIS, width of the RIS affected zones along HAGBs, and the degree of intragranular RIP driven by the RIS mechanism were found distinctly different between the irradiation temperatures. Representative STEM-EDX maps from the irradiation to 23 dpa at 380 °C and RIS profiles at HAGB from all self-ion irradiation conditions are shown in **Figure 5.2-4**.

After the self-ion irradiation to 23 dpa at 380 °C (i.e. at the temperature calculated to match microstructure induced by BOR-60), HAGBs were enriched by Ni, Si and P, depleted by Fe, Cr, Mo and Mn. The level of RIS did not change significantly after 130 dpa and therefore the RIS had reached its steady state at an earlier dose than 23 dpa. The STEM-EDX maps and corresponding RIS profiles depict the segregation trend of solute elements at HAGBs and at the surrounding RIP. The RIS profiles at HAGBs were sharp, ~ 3.5 nm in FWHM for Ni, Si and Fe, ~ 4.5 nm in FWHM for Cr and Mn, and the widest for Mo, ~ 12 nm in FWHM. The boundaries were surrounded by a zone denuded by RIP on each side. These denuded zones were usually 10 – 15 nm in width from boundaries and they had fine RIS characteristics of particular solutes. In general, Ni and Si depleted and Fe, Cr, Mo and Mn enriched the matrix composition within the denuded zone. The distance of the matrix enrichment by Fe was always narrow, ~10 nm, but the distance of the matrix concentrations of Cr, Ni, Si, Mo and Mn affected by RIS was 20 – 30 nm from boundaries. Note, that RIS of Mo and Mn was not always intensive as in **Figure 5.3-6a**, and RIS of these elements at some HAGBs was missing completely. The HAGB enrichment of P present due to thermal treatment seemed to be depleted after irradiations.

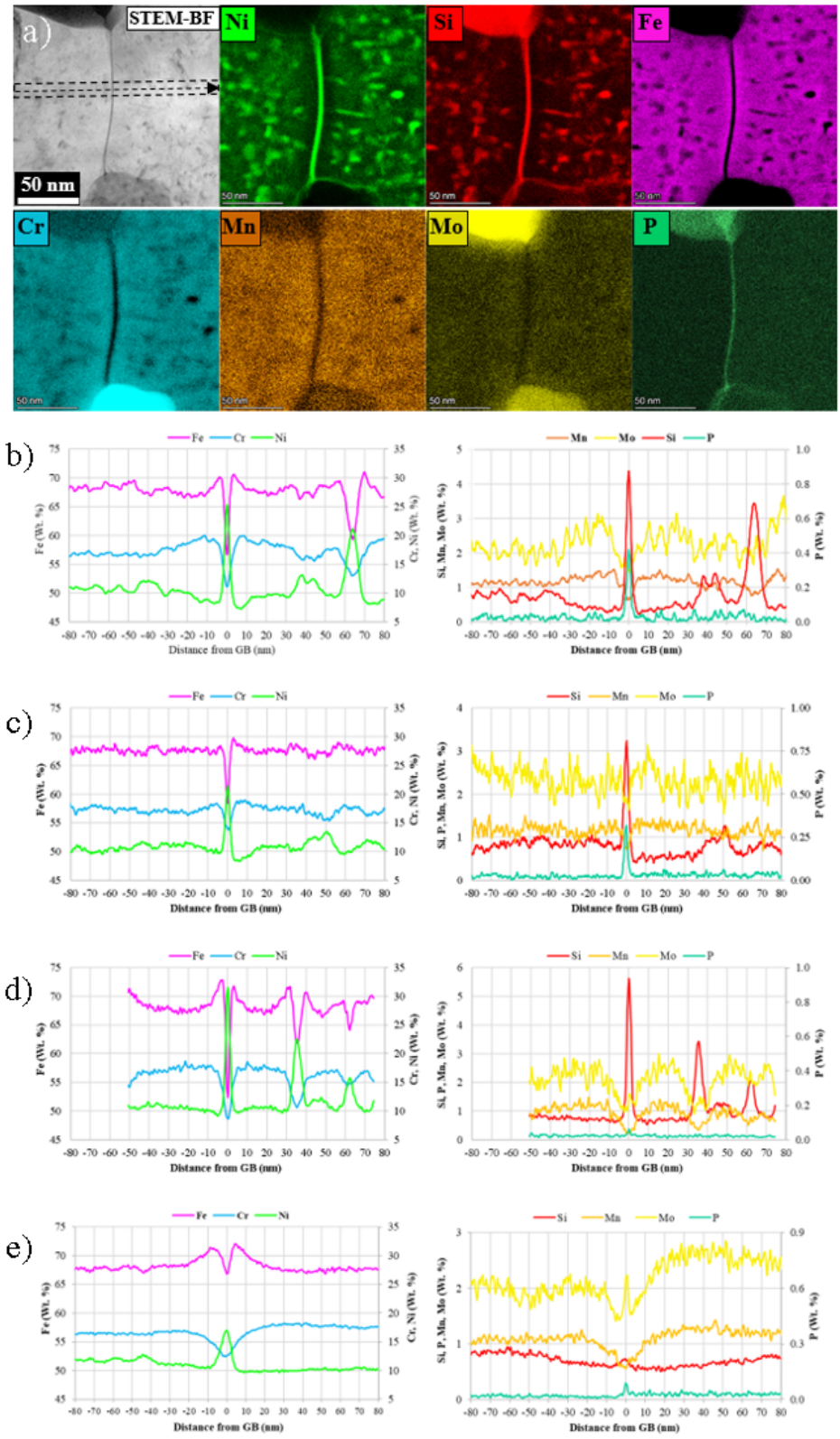

Figure 5.2-4: STEM-EDX elemental mapping after the irradiation to 23 dpa at 380 °C (a) and RIS profiles measured at HAGBs of CW 316 SS Heat B after irradiations to 23 dpa at 380 °C (b), 130 dpa at 380 °C (c), 23 dpa at 500 °C (d) and 15 dpa at 600 °C (e).

After the self-ion irradiation to 23 dpa at temperature 500 °C, the width of RIS profiles at HAGBs and the fine RIS characteristics of particular elements were similar to the 380 °C irradiation, but the average chemical composition at the boundaries showed higher RIS intensity. Differences were found in intragranular RIS, where RIP of average size similar to 380 °C had lower density and RIS was found stronger at dislocations (see Figure 5.3-6c in the *main document*). The similarities in RIS, RIP and Frank loop microstructure ascertained by comparison with the 380 °C irradiations suggest, that the 500 °C irradiation was still in the recombination-dominant regime.

After the self-ion irradiation to 15 dpa at temperature 600°C (i.e. at the temperature calculated to match RIS induced by BOR-60), the composition at HAGB, the width of RIS profile at HAGB and intragranular RIS and RIP were significantly different in comparison with irradiations at lower temperatures. The RIS intensity at 600 °C was suppressed for HAGB concentration of Ni, Si, Fe and P, and only Cr and Mn had similar concentrations as at 380 °C. The STEM-EDX results demonstrate (see Figure 5.3-6d in the *main document* for more details), that the width of RIS profiles was broader, and thus the amount of segregated solute atoms was considerably higher than at lower temperatures. The RIS profile width measured at HAGB in FWHM of segregation peaks was for Ni ~7.4 nm, for Cr ~12 nm, and for Fe was sharper, ~ 3.7 nm. However, Fe was strongly enriching the surrounding matrix by up to ~ 4 wt. % in a zone of 15 – 20 nm in width. Similar behavior to Fe revealed also Mo, which, surprisingly, created a sharp segregation at the HAGB. The RIS behavior of Si was different to RIS of Ni, which was found similar at lower temperature. At this condition, Si segregated with a profile width similar to Ni, but its height was below the matrix composition due to a wide Si depletion zone with a width of ~50 nm from HAGB.

5.2.4 Radiation-induced precipitates

The RIP did not show any diffraction motive in SAED patterns, which would allow unambiguous identification of their crystallographic phase. However, based on the methodology learned during the previous two studies of neutron irradiated samples, the RIP was reliably unveiled via the centered TEM-DF imaging using extra diffraction spots present in SAED patterns of properly tilted austenitic matrix. As it was discussed earlier **[21, 47-49]**, the extra spots correspond with the γ′ (Ni_3Si) phase. To prove this supposition, qualitative chemical composition of the RIP observed in TEM-DF images has been determined via a correlative STEM-EDX elemental mapping, firstly published in **[31]**.

After irradiations to 23 dpa and 130 dpa at 380°C, the TEM-DF imaging with the use of extra spots revealed fine-scale RIP with round or elliptical shape, homogenously dispersed within the matrix. In detail, precipitates were often arranged in chains, likely they would be precipitated on the original dislocations. The RIP nucleation at the pre-existing dislocations agrees with the previous APT measurements of Heat B irradiated by self-ions to 23 dpa **[49]**,

and the γ' precipitation at the original dislocation network of CW 316 SS irradiated by neutrons is reported widely, e.g., from Tihange baffle bolts **[11]**.

In **Figure 5.2-5**, a correlative TEM study of RIP after the irradiation to 23 dpa at 380°C is presented. The centered TEM-DF imaging using extra spots revealed fine RIP with a high contrast against the matrix. The subsequent STEM-EDX elemental mapping of the same area determined Ni-Si-rich precipitates and clusters ("cluster" and "precipitate/RIP" are used interchangeably throughout the next text). Notably, the correlation between TEM-DF and STEM-EDX results clearly showes that particles observed in the TEM-DF image have the same positions as Ni-Si-rich particles in EDX maps (follow red, yellow and purple arrows).

The precipitates were generally found enriched in Ni and Si, depleted in Fe, Cr, Mo and Mn, and with unchanged concentration of P. This result suggests that the observed RIP in TEM-DF images belongs to γ' (Ni_3Si) phase formed via RIS. Qualitative chemical composition of RIP in higher detail is presented via elemental composition profiles in the collected EDX hyperspectral data cubes. Representative profiles performed across three precipitates detected by both TEM-DF and STEM-EDX techniques are presented in **Figure 5.2-5g,h**.

A few Ni-Si-P-rich precipitates can be determined from STEM-EDX maps. The observation of Ni-Si-P-rich RIP may indicate RIP of another phase or radiation-induced clustering of these solute elements. The presence of the Ni-Si-P-rich RIP composition can be interpreted based on APT results from different CW 316 SS irradiated by neutrons, where P-rich clusters were found at the interface of γ' particles **[46]**.

The average size and number density of the RIP was measured from both TEM-DF images and STEM-EDX maps and results for all self-ion irradiation conditions are listed in **Table 5.2-1**. After the irradiation to dose of 23 dpa at 380°C, the RIP average size and density was 5.2 nm and 1.8×10^{22} m^{-3} (measured by TEM-DF) and 8.9 nm and 5.7×10^{22} m^{-3} (measured by STEM-EDX), respectively. These results are not far from the APT study of the Heat B irradiated by self-ions at the same temperature and dose, where Ni-Si precipitates were observed with size of ~4 nm and number density ~1×10^{22} m^{-3} **[49]**. After the dose of 130 dpa at 380°C, the average size and density of the precipitates was 4.1 nm and 1.8×10^{22} m^{-3} (measured by TEM-DF) and 7.9 nm and 4.3×10^{22} m^{-3} (measured by STEM-EDX).

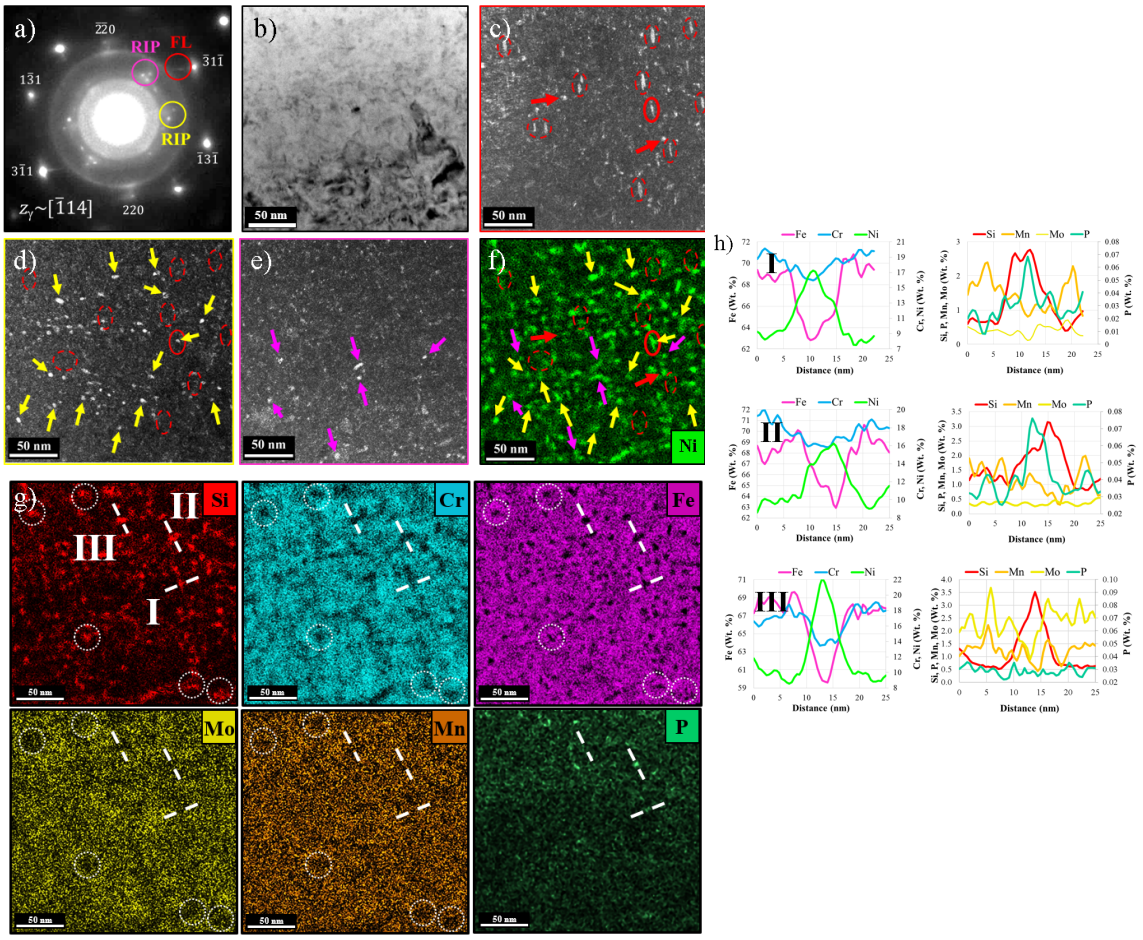

Figure 5.2-5: Correlative TEM of RIP: CW 316 SS Heat B, 5 MeV Fe^{++} irradiation to 23 dpa at 380 °C. SAED of the matrix near [014] pole (a) with extra spots from RIP (marked as RIP) and a "rel-rod" from Frank loops (marked as FL). TEM-BF (b) and TEM-DF of Frank loops (c). TEM-DF of RIP using extra spots marked in (a) by yellow circle (d) and purple circle (e). Ni EDX map of the same area of (b-e) with arrows correlating positions of loops and RIP observed in (c-e). The color of arrows corresponds with colors of the used TEM-DF conditions marked in (a). The remaining STEM-EDX maps of the area (g), the circles are pointing to areas with depleted Mo and Mn due to RIS, the bars are representing chemical profiles on selected RIP. RIP chemical composition profiles (h) marked in (g).

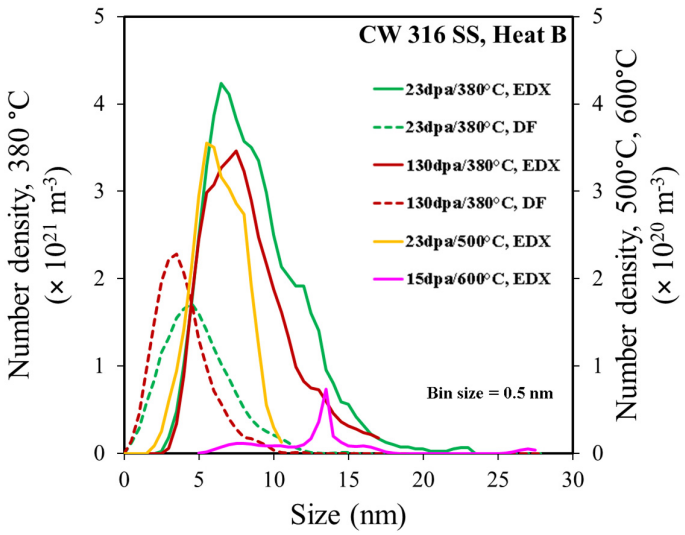

Figure 5.2-6: Size distribution of Ni-Si rich RIP in CW 316 SS Heat B irradiated by 5 MeV self-ions at different temperatures and doses. DF = TEM-DF measurement, EDX = STEM-EDX measurement.

The RIP average size and density have very similar values after irradiations to 23 and 130 dpa at 380 °C (considering results obtained by TEM-DF or STEM-EDX). Also, the RIP size distribution (**Figure 5.2-6**) showed similar results of RIP. It indicates that the population of RIP has been already saturated at the dose of 23 dpa. Considering that the RIP formation is driven by RIS of solutes at lattice sinks, the steady state could arise even earlier at a dose below 10 dpa corresponding with the saturation dose of the solute RIS at grain boundaries **[67]**.

After the self-ion irradiation at 500°C to 23 dpa, the RIP was not observed by the TEM-DF imaging successfully. However, RIP was ascertained from STEM-EDX maps, **Figure 5.2-7**. The RIP average size was measured 6.6 nm and the RIP was dispersed more sparsely within the matrix. The number density measured from EDX maps was ~0.3×10^{22} m^{-3}, what is more than one order of magnitude less than after the 380 °C irradiation. The precipitates or clusters were enriched in Ni and Si, depleted in Fe, Cr, Mo and Mn. RIP enrichment by P has not been detected at this temperature. It means that both the RIP average size and the composition was similar at the 500 °C irradiation as at the 380°C one. The qualitatively similar RIP composition influenced by RIS further indicates that particles observed in EDX maps are of the γ' phase. The enrichment in Mn or P has not been found in any case of RIP measurement at this temperature, even though nucleation of G-phase was observed in CW 316 SSs irradiated by neutrons at this temperature **[68-70]**.

After the self-ion irradiation at 600 °C to 15 dpa, the radiation-induced microstructure and microchemistry, including RIP, appeared very different from irradiations at 380 °C and 500 °C. This is documented by STEM-EDX maps in **Figure 5.2-8**. The precipitates were large, with average size ~13.6 nm and the largest particles often exceeded 20 nm. The RIP was dispersed very sparsely and randomly within the austenitic matrix. The RIP density could be measured only if the particles appeared in STEM-EDX maps and it was roughly estimated to

be ~0.03×10^{22} m^{-3}, what is one or more than two orders of magnitude lower density than after 500 °C or 380 °C irradiations, respectively. All particles were enriched only in Ni and Si, depleted in Cr, Fe, Mo, and with unaltered Mn and P. It indicates that RIP formation at 600 °C was driven by the RIS mechanism as well as at the lower temperatures and it can be expected in the form of γ' phase. The RIP enrichment in Mn or P or the nucleation of G-phase has not been observed at this temperature.

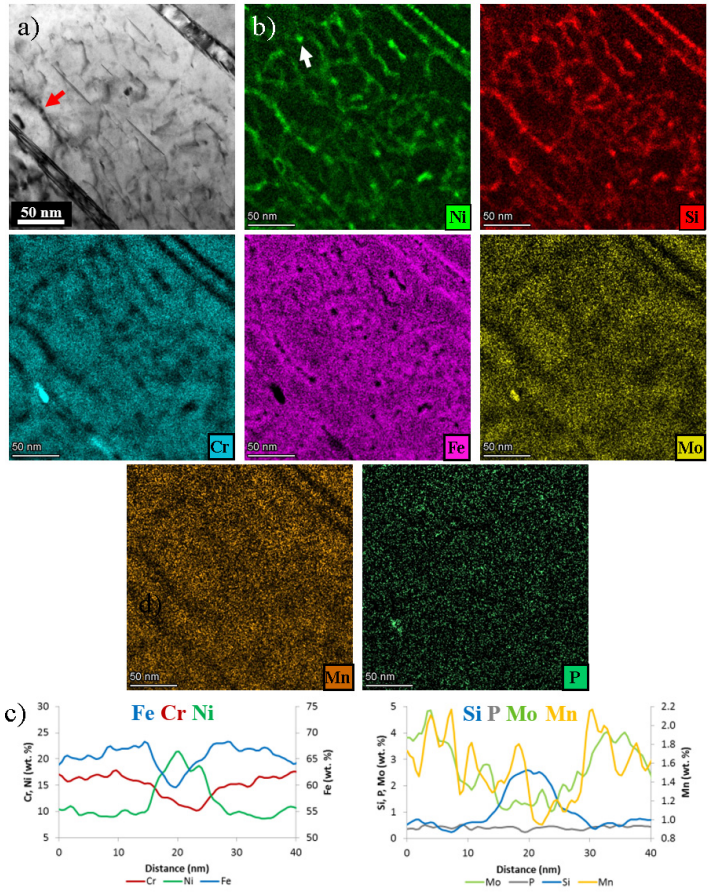

Figure 5.2-7: CW 316 SS Heat B, 5 MeV Ni^{++} irradiation to 23 dpa at 500 °C. A STEM-BF image (a) shows large edge-on Frank dislocation loops, micro-twins and edge on twin boundaries (top right) and a dislocation wall (marked by arrow). The STEM-EDX maps (b) corresponding to (a) reveal Ni-Si rich RIP and RIS at dislocation microstructure and edge-on twin boundaries. An example of composition profile of one RIP (b) marked by arrow in (a) and revealing its Ni-Si enrichment and Fe, Cr, Mo and Mn depletion.

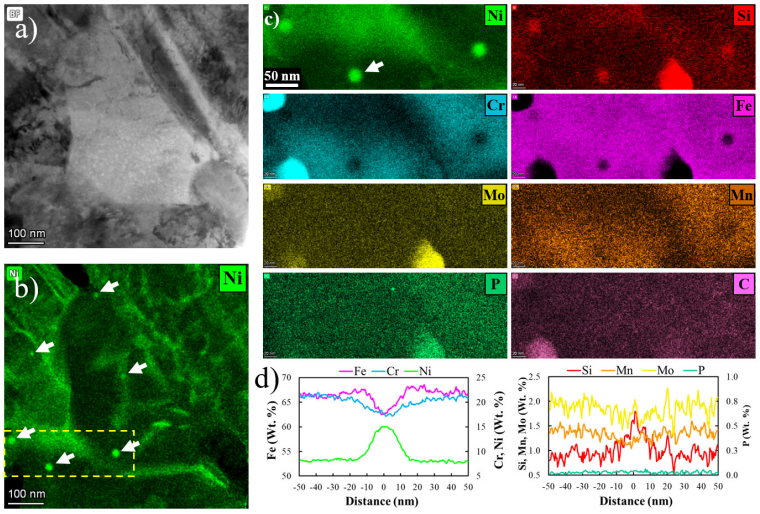

Figure 5.2-8: CW 316 SS Heat B, 5 MeV Fe^{++} irradiation to 15 dpa at 600 °C. STEM-BF image (a) and corresponding STEM-EDX Ni map with indicated RIP by arrows (b). A detail chemical mapping of RIP (c) corresponding with the area marked by a yellow rectangle in (b). Chemical composition profile (d) of the precipitate marked by arrow in (c).

5.2.5 Benchmark of self-ion and neutron irradiations

The comprehensive TEM analysis of the microstructure and microchemistry of the CW 316 SS Heat B was performed after all self-ion irradiation conditions and it was surveyed in the previous chapter. The main TEM results are summarized in **Table 5.2-1** and graphically benchmarked in **Figure 5.2-9** together with the data from the Heat B irradiated in BOR-60 to doses of 25 and 46 dpa at 320 °C **[16, 17]**. The benchmark is comparing measures of Frank dislocation loops, cavities, radiation-induced precipitates and radiation-induced segregation of solutes at high-angle grain boundaries. Note, that the RIP data were not achieved by the TEM-DF measurement at 500 °C and 600 °C condition, and they are substituted by the results from STEM-EDX measurements.

Very importantly, the benchmark reveals that single self-ion irradiations to the intermediate (23 dpa) and the high (130 dpa) dose at 380 °C were capable to produce all types of the radiation-induced damage with measures close to the data from BOR-60 irradiations.

In particular, very close match was in Frank loop average size, RIP average size and density, and RIS of Si, Cr, P and Mo. The measure with larger difference was Frank loop density, which was ~3.7× higher after 25 dpa in BOR-60 than after 23 dpa by self-ions. However, results of the Frank loop density from 380 °C irradiations are still considerably closer to neutrons than from self-ion irradiations at higher temperatures. The similar Frank loop microstructure produced in the Heat B by self-ions at 380 °C and by BOR-60 at 320 °C is documented from the 23 dpa and 25 dpa dose of these irradiations in **Figure 5.2-10**.

The RIP in the form of γ' phase determined in Heat B had very similar average size, number density and morphology after BOR-60 irradiations to 25 and 46 dpa at 320 °C and both self-ion irradiations at 380 °C. Microstructure of the γ' precipitates after neutron and self-ion irradiations to 25 dpa and 23 dpa, respectively, is presented in **Figure 5.2-11**.

The results of the phase, average size and density after self-ion irradiations to 23 and 130 dpa at 380°C are in good agreement with literature data from other CW 316 SSs irradiated by neutrons at PWR-relevant temperatures **[11, 17, 26, 44-47]**. The average size agrees with γ' precipitates determined by TEM and APT in baffle-bolts irradiated to 12 dpa at 343 – 365°C **[11, 46]** and FTT segments irradiated to 74 dpa at 305°C **[26, 45]**. The comparison with neutron irradiated CW 316SS in FBR environment shows that the FBR irradiations in BOR-60 **[17]** and SM **[21]** experiments at temperatures 300 – 320°C produced γ' precipitates with similar average size and density as self-ion irradiation, but the Phoenix FBR irradiation at higher temperature of 380 °C to dose 31 dpa **[71]** produced γ' and also G-phase precipitates with substantially bigger average size than the self-ion irradiation.

The G-phase precipitates are likely to be present in CW 316 SS at higher temperatures and/or neutron doses. The Mn segregation to Ni-Si-Mn-rich precursors of the G-phase is not driven by RIS, which depletes Mn atoms at sinks, but it is accounted for a process activated by thermodynamic driving force **[45]**, which requires higher nucleation dose and/or temperature. This agrees with results from the PWR irradiated FTT material, in which the Ni-Si-Mn-rich clusters aside the Ni-Si-rich clusters had been ascertained by APT from dose of 74 dpa at 305 °C **[45]**. However, Ni-Si-Mn-rich clusters or precipitates have not been ascertained via STEM-EDX or TEM-DF in the Heat B irradiated by self-ions neither after the high dose of 130 dpa at 380 °C, nor after 500 °C or 600 °C irradiations. This can be attributed to instability of the G-phase due to the effect of ballistic mixing **[25]** on dissolution of potentially formed Ni-Si-Mn clusters during self-ion irradiations with high damage rate, resulting in re-formation of Ni-Si clusters due to the RIS depleting Mn at sinks.

The absence of cavities in the Heat B after self-ion irradiations is consistent with BOR-60 irradiations, and it means that both irradiations were equivalent in terms of present types of radiation damage entering to the microstructure degradation of the material. A presence of cavities would change the mutual interplay between evolving radiation defects and it is worth noting that this aspect is the main difference between the radiation damage evolved during irradiations performed by the self-ions and by thermal neutrons in a PWR.

Another measure with larger difference is RIS of Fe and Ni at HAGB, for which the 380 °C irradiation produced higher concentrations, however, 600 °C irradiation matched well HAGB concentrations of Fe, Cr and Ni with the BOR-60 irradiations. Even though the 600 °C irradiation to 15 dpa produced HAGB composition with better match for the majority of solutes than irradiations at lower temperatures, this condition produced very different Frank loop and RIP microstructure and also considerably wider segregation RIS profiles at HAGB in comparison with BOR-60 irradiations **[16, 17]**. The 500 °C irradiation produced RIS and composition at HAGB similar to the 380 °C irradiation, however, it produced Frank loops with

average size and density with measures far from the BOR-60 irradiations. Therefore, only results from 380 °C irradiations are further considered for more detailed benchmarks with the BOR-60 irradiations and also PWR irradiations of other CW 316 SSs.

The RIS at HAGB of the CW 316 SS Heat B after the self-ion irradiations at 380 °C was found with trend typical for neutron irradiated CW 316 steels, when HAGB were enriched only by Ni and Si in comparison with the as-received state. The measured depletion of the thermally enriched concentration of P at HAGBs in the as-received state was similar as after BOR-60 irradiations. In **Figure 5.2-12**, STEM-EDX profiles of solute RIS at HAGB of the Heat B irradiated by the self-ions to 23 dpa and by the BOR-60 to 25 dpa are compared along with RIS profiles at HAGB of the different CW 316 SS from FTT irradiated in PWR to 25 dpa **[26]**. The profile after the BOR-60 irradiation was with lower segregation of Ni, Cr and Si, however, a close match was found in segregation of Ni and Cr between the self-ion and PWR irradiation. All three irradiations revealed segregation profiles with similar width, only Si was narrower for PWR conditions. RIS at HAGB with very similar profiles of Fe, Ni, Cr and Si to the profiles from self-ion irradiations at 380 °C can be found from the Tihange PWR baffle bolt irradiated to 13 dpa at 343 °C **[11]**. The presented RIS profiles in **Figure 5.2-12** are further compared with results from the 600 °C self-ion irradiation to 15 dpa. It demonstrates, that this temperature, originally calculated by the Mansur's invariant theory **[27]** to match the BOR-60 induced RIS with the high dose rate ion irradiation, was not appropriate.

The good match of microstructure (Frank loops and RIP) and microchemistry (the magnitude of RIS of Cr, Ni and Si) achieved in the CW 316 SS between irradiations by self-ions at 380 °C and fast neutrons at 320 °C can be explained with a high density of sinks in this material. In the extreme condition of very high sink density, Mansur **[27]** has predicted that there should be no temperature shift needed to compensate the dose rate difference from the neutron irradiation. Interestingly, similar results were obtained in self-ion irradiated ferritic-martensitic steel HT9 **[28, 29]**, where very good match with neutrons was achieved with temperature shift lower than 20 °C. Similarly to the CW 316 SS, this material has a high sink density, and it implies that the high sink density can be the key condition for the successful emulation of the neutron induced radiation damage by a single self-ion irradiation.

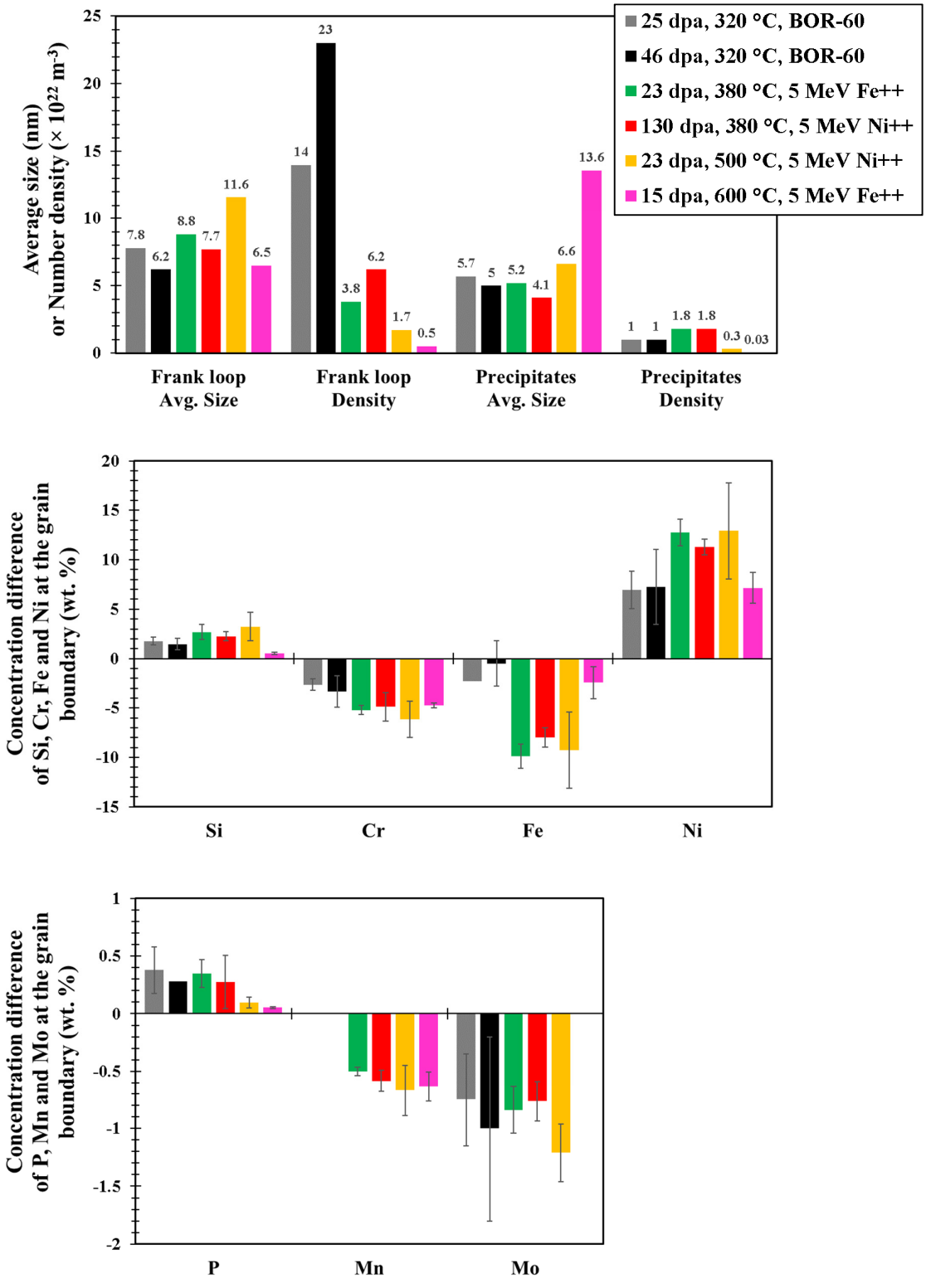

Figure 5.2-9: Benchmark of Frank loops, RIP, and RIS at HAGB in CW 316 SS Heat B after BOR-60 **[16, 17]** and performed 5 MeV self-ion irradiations.

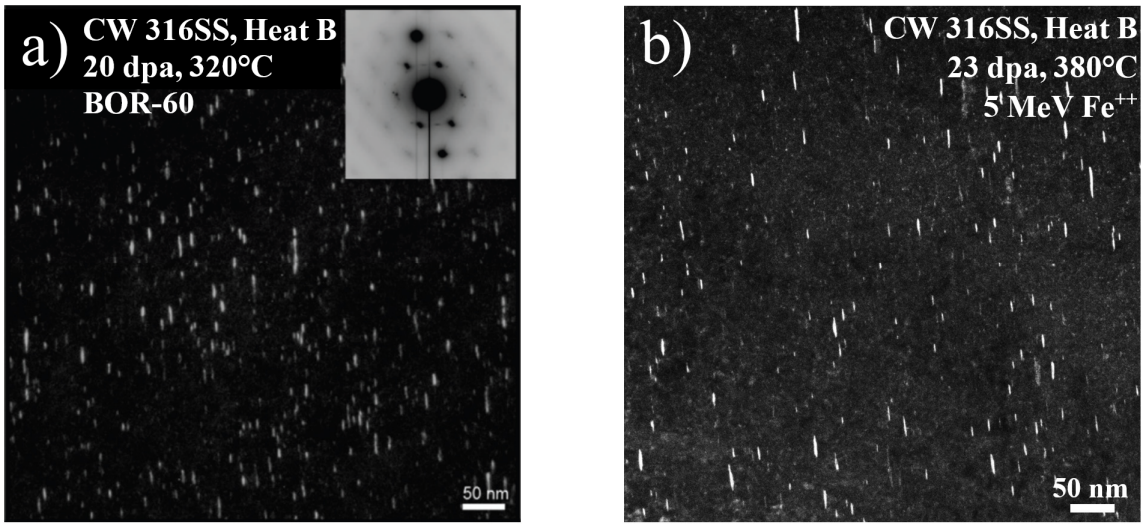

Figure 5.2-10: TEM-DF "rel-rod" images of edge-on Frank loops in the CW 316 SS Heat B after the BOR-60 **[20]** (a) and the self-ion (b) irradiation.

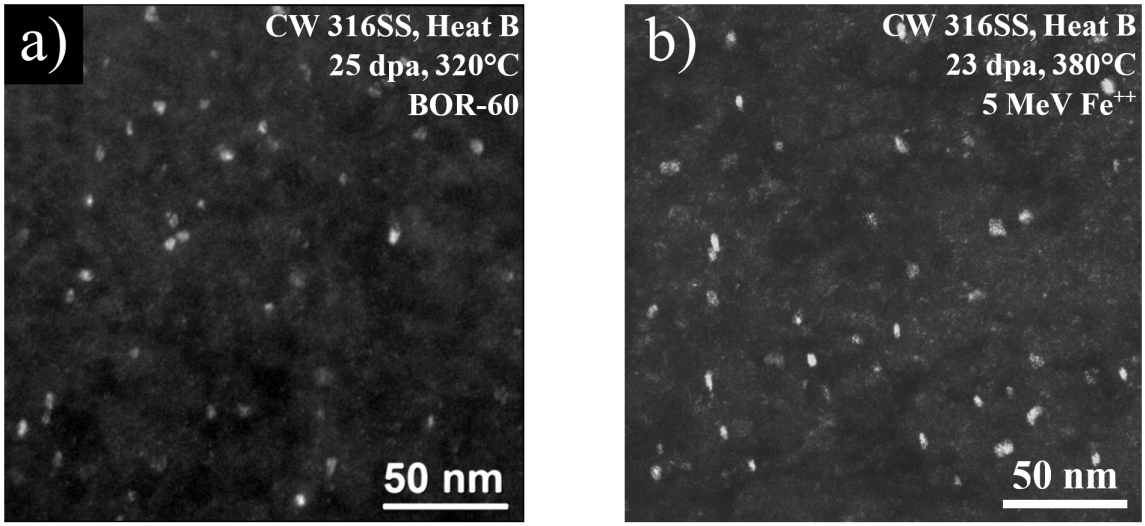

Figure 5.2-11: TEM-DF images of γ' RIP in the CW 316SS Heat B after the BOR-60 **[16]** (a) and the self-ion (b) irradiation.

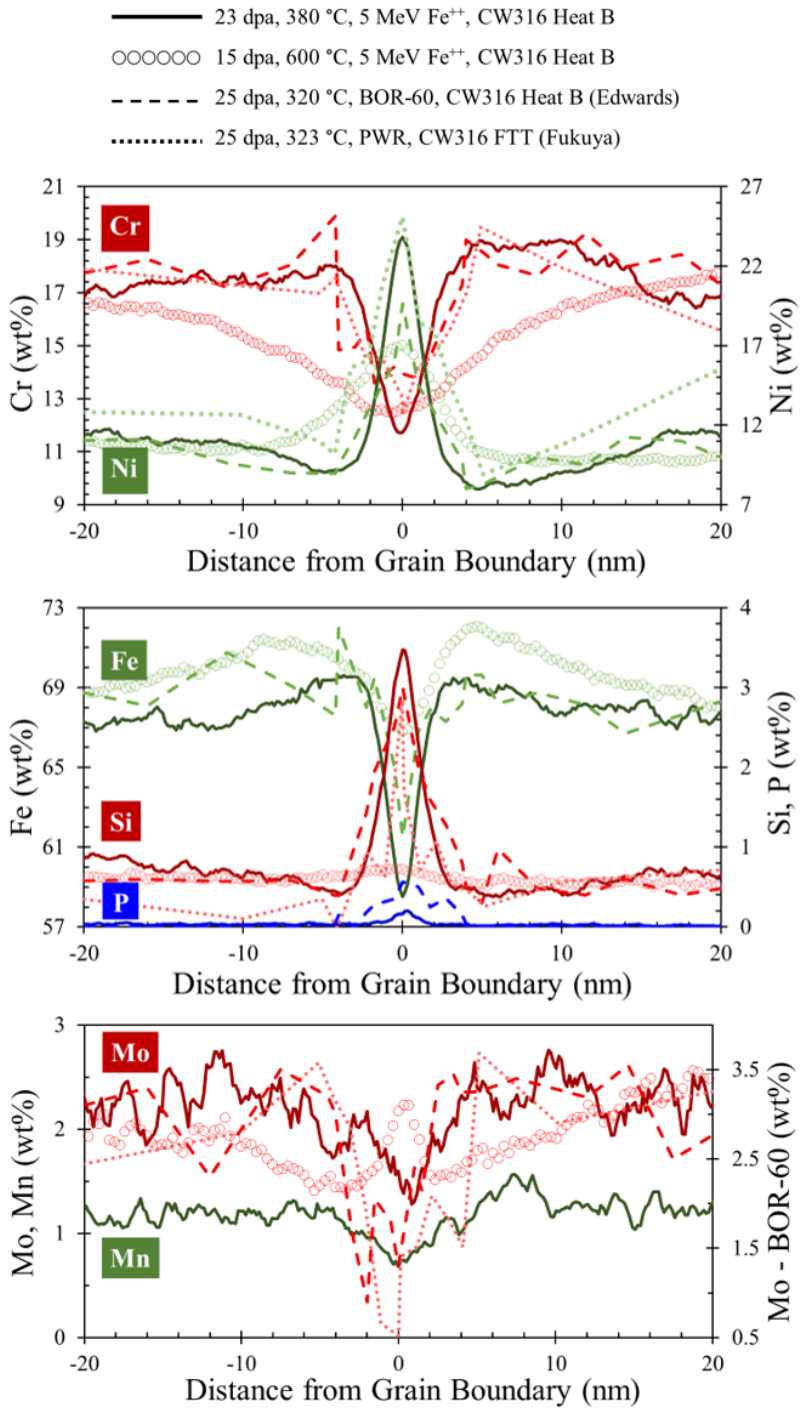

Figure 5.2-12: RIS profiles measured by STEM-EDX at HAGB of CW 316 SS Heat B irradiated by self-ions at 380 °C to 23 dpa and at 600 °C to 15 dpa, and by BOR-60 at 320 °C to 25 dpa [16, 57]. Data are compared with the CW 316 FTT irradiated by a PWR at 323 °C to 25 dpa [26].

The new results from the comprehensive TEM investigation of the radiation-induced damage in the self-ion irradiated CW 316 SS Heat B can be further graphically benchmarked with results from all BOR-60 irradiation doses covering the range from 5.5 to 46 dpa, and with extensive results from the only available CW 316 SS FTT material irradiated in a PWR to doses from 3 up to 100 dpa, i.e., to the high dose relevant to the PWR life-time extension to 60 years. The FTT irradiation temperatures were between 293 and 323 °C and the dose rates were from 8×10^{-9} to 1.5×10^{-7} dpa/s **[26, 45, 72]**. Nevertheless, it is necessary to be recalled that the FTT material was different CW 316 of from the Heat B, *e.g.,* in slightly different chemical composition or lower cold-working of 15%.

The complex benchmark of all three irradiated materials is in **Figure 5.2-13**. It reveals, that the average size of Frank loops and RIP after self-ion irradiations is circa in-between two neutron irradiations, while BOR-60 developed slightly smaller Frank loops and slightly larger RIP in the Heat B than PWR in the FTTs. If the distinct difference in Frank loop density was found between self-ion and BOR-60 irradiations, this measure matched very closely between self-ion and PWR irradiations. RIP density was fairly equivalent for all three irradiation types, if the precipitates were measured from TEM-DF images.

The RIS measured at HAGBs after all three types of irradiation is benchmarked for all solute elements of interest in **Figure 5.2-13b**. In comparison to self-ions, BOR-60 irradiations produced less intense RIS of Ni and Cr and comparable RIS of Mo, Si and P. On contrary, a close match was found between self-ion and PWR irradiations, which produced RIS with almost the same results for Ni, Cr and Si.

All self-ion, BOR-60 and PWR irradiations revealed saturation behavior in measures of each radiation damage type studied in this work. In addition, these measures did not reveal substantial changes between the intermediate dose and the very high dose of the self-ion irradiation and they followed up the steady-state trend as neutron irradiations. By considering this, the obtained self-ion irradiation data suggest that degradation of CW 316 SS alloys may not evince substantial changes induced by the radiation damage at high doses relevant to 60+ operational years of PWR reactors.

However, the self-ion and fast neutron irradiations did not emulate formation of gas filled cavities due to no or very low He production rate, respectively. Since the generation of both gases is induced during whole PWR operational life, a continuous cavity evolution can be expected, which will play an additional role in the co-evolution interplay with the other types of radiation damage, particularly at high doses.

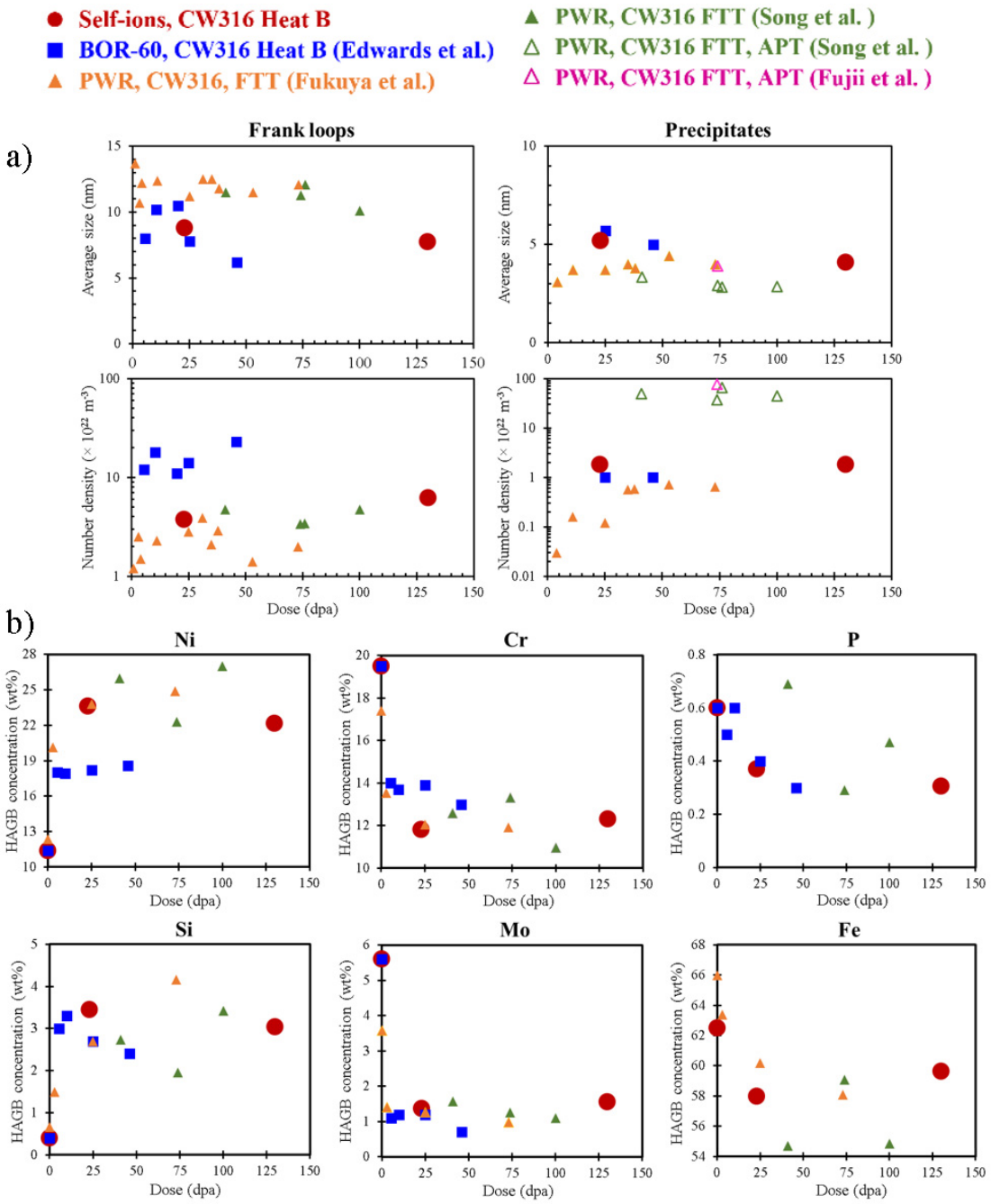

Figure 5.2-13: Benchmark of average size and density of Frank loops and RIP (a), and RIS at HAGB (b) in the CW 316 SS Heat B irradiated by self-ions at 380 °C and in BOR-60 at 320 °C **[17]** and in the CW 316 SS of FTT irradiated in PWR at 300 – 320 °C **[26, 45, 72]**.

6 Conclusions

With respect to the three established objectives for this doctoral thesis, the main outcomes from the performed investigations can be summarized in the following points:

1. The TEM analysis of radiation-induced microstructure (i.e., Frank dislocation loops, RIP and cavities) was performed on the PWR baffle bolt made of 08Ch18N10T austenitic stainless steel extracted from the commercial WWER-440 Greifswald reactor, which was decommissioned after 15 years of operation. Neutron irradiation under real in-service conditions accumulated dose of 11.4 dpa in the head of the bolt, but significant gradients of irradiation temperature (increased by gamma heating) and dose rate caused non-uniform evolution of the radiation-induced damage along the length of the bolt.

The gradients were studied at three positions along the shank of the bolt. The microstructural analysis revealed the most obvious difference in the He-filled cavities with substantially increasing average size and decreasing density in the direction from the bolt head to the end of the shank. This direction corresponds to the temperature maximum and dose rate minimum at the end of the shank. The increased cavity growth is consistent with the known effect of higher temperature and lower dose rate on the cavity formation. At the end of the shank, where the temperature maximum was ~400 °C, predominantly large cavities with the average size of ~7 nm and the number density of 2.3×10^{21} m^{-3} caused the highest level of volumetric swelling along the bolt, 0.04 %. The increase in temperature also caused the higher abundance of RIP, but the Frank dislocation loop microstructure and radiation hardening along the shank remained unchanged.

The increased cavity formation and swelling due to the gamma heating can be classified as the main concern regarding the long-term evolution of the radiation damage influencing aging issues (IASCC susceptibility) of baffle bolts of the particular reactor type.

2. The TEM analysis of the radiation-induced microstructure was performed on the PWR baffle bolt material of CW 316 SS irradiated in the SM experimental reactor to dose of 15 dpa at the temperature of 300 °C by the flux of neutrons with fast spectrum (emulating the FBR irradiation) and by the flux of neutrons with mixed spectrum (emulating the PWR irradiation). The experiment was conducted with aim to investigate the influence of irradiation neutron spectra on IASCC susceptibility and to assess the relevance of using FBR irradiations in IASCC material testing programs.

The TEM revealed very similar Frank dislocation loop and RIP measures after both irradiations, but significantly higher density of nano-cavities, cavity denuded zones along grain boundaries and cavities at grain boundaries after the mixed spectrum irradiation.

This observation was discussed in detail and attributed to the synergy of vacancy flux associated with solute RIS at boundaries, effect of He concentration on cavity nucleation and growth enhancement, and effect of Ni RIS profile on non-uniform He production rate via Ni transmutations. This observation is also consistent with the up to 35 times faster He production rate of the mixed spectrum and it suggests a stronger correlation of helium production rates with IASCC susceptibility. This was further supported by SSRT tests, which showed IASCC susceptibility in the form of significantly higher percentage of IG cracking of SSRT specimens irradiated by the mixed spectrum compared to those irradiated by the fast spectrum.

3. 5 MeV Ni^{++} or Fe^{++} self-ion irradiations to 23 dpa and 130 dpa at 380 °C, 23 dpa at 500 °C, and 15 dpa at 600 °C were performed on the PWR baffle bolt material of CW 316 SS (Heat B) at the Michigan Ion Beam Laboratory to emulate radiation-induced microstructure and microchemistry (i.e., RIS at solute sinks) as produced in the same material fast neutron irradiations in BOR-60 reactor at 320 °C and doses up to 46 dpa.

To evaluate the emulation, samples from each self-ion irradiation condition were comprehensively examined with the state-of-the-art TEM and advanced novel TEM techniques to determine all types of the radiation damage. Complex benchmarks of the radiation damage data from self-ion and BOR-60 irradiations were then carried out.

It was demonstrated, that both radiation-induced microstructure and microchemistry in the CW 316 SS can be successfully emulated by a single self-ion irradiation. This was achieved by irradiation at 380 °C, although it was calculated by the Mansur's invariant equations, that this temperature will only match the microstructure, while the temperature 600 °C will only match the microchemistry. Despite the large difference in dose rates, $\sim 10^{-3}$ dpa/s for self-ions and $\sim 5\times10^{-7}$ dpa/s for fast neutrons, the relatively small temperature shift of 60 °C was sufficient to emulate all complex radiation damage. The results of RIS at HAGB and within the austenitic matrix in the form of Ni-Si rich RIP at the primary dislocation network indicated, that the high sink density of this material created by the cold work played a crucial role in the evolution of the complex radiation damage. Furthermore, a very high sink density is suggested by Mansur as a limiting condition when no temperature shift is needed to compensate for the dose rate differences.

As a result, the high sink density was essential for the successful self-ion emulation of the high dose neutron irradiation, and in general, the sink density turned out to be the critical factor in determining the temperature shifts and successful neutron irradiation emulations with self-ions.

7 References

[1] S.J. ZINKLE, G.S. WAS, Materials challenges in nuclear energy, *Acta Materialia*, Volume 61, Issue 3, 2013, p. 735-758.

[2] S.M BRUEMMER, E.P SIMONEN, P.M SCOTT, P.L ANDRESEN, G.S WAS, J.L NELSON, Radiation-induced material changes and susceptibility to intergranular failure of light-water-reactor core internals, *Journal of Nuclear Materials*, Volume 274, Issue 3, 1999, p. 299-314.

[3] E. A. KENIK, J. T. BUSBY, Radiation-induced degradation of stainless steel light water reactor internals, *Materials Science and Engineering: R: Reports*, Volume 73, Issues 7–8, 2012, p. 67-83.

[4] F.A. GARNER, 4.02 – Radiation Damage in Austenitic Steels, Editor(s): Rudy J.M. Konings, *Comprehensive Nuclear Materials*, Elsevier, 2012, p. 33-95.

[5] G.E. LUCAS, The evolution of mechanical property change in irradiated austenitic stainless steels, *Journal of Nuclear Materials*, Volume 206, Issues 2–3, 1993, p. 287-305.

[6] G.E. LUCAS, M. BILLONE, J.E. PAWEL, M.L. HAMILTON, Implications of radiation-induced reductions in ductility to the design of austenitic stainless steel structures, *Journal of Nuclear Materials*, Volumes 233–237, Part 1, 1996, p. 207-212.

[7] G.S. WAS, P. ANDRESEN, Irradiation assisted corrosion and stress corrosion cracking (IAC/IASCC) in nuclear reactor systems and components, *Nuclear Corrosion Science and Engineering*, 2012, p. 131-185.

[8] P.L. ANDRESEN, G.S. WAS, 5.08 – Irradiation Assisted Stress Corrosion Cracking, Editor(s): Rudy J.M. Konings, *Comprehensive Nuclear Materials*, Elsevier, 2012, p. 177-205.

[9] International Atomic Energy Agency, Nuclear Power Reactors in the World, Reference Data Series No. 2, *IAEA*, Vienna, 2012, 79 pages.

[10] US Department of Energy, Light Water Reactor Sustainability Program: Integrated Program Plan, US Department of Energy, Office of Nuclear Energy, 2012.

[11] D.J EDWARDS, E.P SIMONEN, F.A GARNER, L.R GREENWOOD, B.M OLIVER, S.M BRUEMMER, Influence of irradiation temperature and dose gradients on the microstructural evolution in neutron-irradiated 316SS, *Journal of Nuclear Materials*, Volume 317, Issue 1, 2003, p. 32-45.

[12] F.A. GARNER, L.R. GREENWOOD, Survey of Recent Developments Concerning the Understanding of Radiation Effects on Stainless Steels Used in the LWR Power Industry. *Proceedings of 11th International Conference on Environmental Degradation of Materials in Nuclear Power systems – Water Reactors*, 2003, p. 887-910.

[13] M. ERNESTOVA, A. HOJNA, E. KEILOVA, J. KOCIK, J. MICHALICKA, Results on irradiated austenitic stainless steel bolts of reactor core internals. *Proceedings of International Symposium Fontevraud VII,* CDROM, Paper A053, Societe Francaise dEnergie Nucleaire, France, 2010.

[14] J. MICHALICKA, A. HOJNA, E. KEILOVA, J. KOCIK, TEM radiation damage investigation of neutron irradiated baffle-to-former bolt extracted from a decommissioned WWER-440 reactor. *Proceedings of the 16th International Conference on Environmental Degradation of Materials in Nuclear Power Systems – Water Reactors*, CDROM, The Minerals, Metals & Materials Series, 2013.

[15] A.V. KARASIOV, L.R. GREENWOOD, Neutron flux spectra and radiation damage parameters for the Russian BOR-60 and SM-2 reactors, (DOE/ER–0313/17). United States, 1995.

[16] D.J. EDWARDS, E.P. SIMONEN, S.M. BRUEMMER, Characterization of Neutron-Irradiated 300-Series Stainless Steels (EP-P14516/C7130), *EPRI*, Palo Alto, CA, 2006.
[17] D.J. EDWARDS, S.M. BRUEMMER, Characterization of CIR II Irradiated Stainless Steels (EP-P19021/C9406), *EPRI*, Palo Alto, CA, 2008.
[18] J. P. MASSOUD, P. DUBUISSON, P. SCOTT, N. LIGNEAU, E. LEMAIRE, The effects of neutron radiation on materials for core internals of PWRs. *Proceedings of International Symposium Fontevraud V,* Societe Francaise dEnergie Nucleaire, 2002, p. 417.
[19] J.P. MASSOUD, M. ŽAMBOCH, P. BRABEC, V. K. SHAMARDIN, V. I. PROKHOROV, PH. DUBUISSON, Influence of the neutron spectrum on the tensile properties of irradiated austenitic stainless steels, in air and in PWR environment. *Proceedings of the 12th International Conference on Environmental Degradation of Materials in Nuclear Power System – Water Reactors*, The Minerals, Metals & Materials Society, 2005, p. 357-363.
[20] D. EDWARDS, E. SIMONEN, S. BRUEMMER, P. EFSING, Microstructural Evolution in Neutron-Irradiated Stainless Steel: Comparison of LWR and Fast-Reactor Irradiations. *Proceedings of the 12th International Conference on Environmental Degradation of Materials in Nuclear Power System – Water Reactors*, The Minerals, Metals & Materials Society, 2005, p. 419-428.
[21] M. ERNESTOVÁ, J. BURDA, J. KOČÍK, E. KEILOVÁ, J. MICHALIČKA, C. POKOR, Influence of the neutron spectrum on the sensitivity to IASCC and microstucture of CW 316 material. *Proceedings of International Symposium Fontevraud VIII*, CDROM, Paper 102_T02, Societe Francaise dEnergie Nucleaire, France, 2014.
[22] G.S. WAS, *Fundamentals of Radiation Materials Science, Metals and Alloys*, Springer Science+Business Media New York, 2017. ISBN 978-1-4939-3438-6.
[23] G.S. WAS, R.S. AVERBACK, 1.07 – Radiation Damage Using Ion Beams, Editor(s): Rudy J.M. Konings, *Comprehensive Nuclear Materials*, Elsevier, 2012, p. 195-221.
[24] G.S. WAS, T. ALLEN, Intercomparison of microchemical evolution under various types of particle irradiation, Journal *of Nuclear Materials*, Vol. 205, 1993, p. 332-338.
[25] G. MARTIN, Phase stability under irradiation: Ballistic effects, *Physical Review B*, Volume 30, Number 3, 1984, p. 1424-436.
[26] International Atomic Energy Agency, Assessment and management of ageing of major nuclear power plant components important to safety: PWR vessel internals, *IAEA*, Vienna, 1999, ISSN 1011–4289.
[27] L.K. MANSUR, Theory of transitions in dose dependence of radiation effects in structural alloys, *Journal of Nuclear Materials*, Vol. 206, Issues 2–3, 1993, p. 306-323.
[28] G.S. WAS, Z. JIAO, E. GETTO, K. SUN, A.M. MONTERROSA, S.A. MALOY, O. ANDEROGLU, B.H. SENCER, M. HACKETT, Emulation of reactor irradiation damage using ion beams, *Scripta Materialia*, Volume 88, 2014, p. 33-36.
[29] E. GETTO, Z. JIAO, A.M. MONTERROSA, K. SUN, G.S. WAS, Effect of irradiation mode on the microstructure of self-ion irradiated ferritic-martensitic alloys, *Journal of Nuclear Materials*, Volume 465, 2015, p. 116-126.
[30] Z. JIAO, J. MICHALICKA, G.S. WAS, Self-ion emulation of high dose neutron irradiated microstructure in stainless steels, *Journal of Nuclear Materials*, Volume 501, 2018, p. 312-318.
[31] J. MICHALIČKA, Z. JIAO, G.S. WAS, Radiation-induced precipitates in a self-ion irradiated cold-worked 316 austenitic stainless steel used for PWR baffle bolts. *Proceedings of 18th International Conference on Environmental Degradation of Materials in Nuclear Power Systems – Water Reactors*, Minerals, Metals and Materials Series, Volume Part F9, 2018, P. 565-580.

[32] J. MICHALIČKA, Z. JIAO, G.S. WAS, Radiation Damage in a CW 316 Austenitic Stainless Steel Irradiated by Self-ions at High Doses and Temperatures: Comparison with FBR and PWR Irradiations. *Proceedings of 21st International Conference on Environmental Degradation of Materials in Nuclear Power Systems – Water Reactors*, 2023, St. John's, Newfoundland, Canada, August 6-10, 2023.
[33] M.L. JENKINS, M.A. KIRK, *Characterization of Radiation Damage by Transmission Electron Microscopy*, Series in Microscopy in Materials Science, CRC Press, London, UK, 2001. ISBN-10: 075030748X.
[34] S.J. PENNYCOOK, P.D. NELLIST, *Scanning Transmission Electron Microscopy, Imaging and Analysis*, Springer New York Dordrecht Heidelberg London, 2011. ISBN 978-1-4419-7199-9.
[35] R.F. EGERTON, *Electron Energy-Loss Spectroscopy in the Electron Microscope*, Third Edition, Springer Science+Business Media, LLC, 2011. ISBN 978-1-4419-9582-7.
[36] J. RATAJ, Výpočet fluencí Greifswald, internal protocol ÚJV Řež, October 2004 (in Czech)
[37] E.P. SIMONEN, F.A. GARNER, N.A. KLYMYSHYN, M.B. TOLOCZKO, Response of PWR Baffle-Former Bolt loading to swelling, irradiation creep and bolt replacement as revealed using finite element modeling. *Proceedings of the 12th International Conference on Environmental Degradation of Materials in Nuclear Power System – Water Reactors*, The Minerals, Metals & Materials Society, 2005.
[38] L. PECINKA, P. MACAK, Calculation of temperature and stress field in bolts and core shroud of VVER 440/230 Loviisa, Report DITI 300/327, NRI Rez plc, Czech Rep., November 2007 (in Czech)
[39] F.A. GARNER, D.J. EDWARDS, S.M. BRUEMMER, S.I. POROLLO, YU.V. KONOBEEV, V.S. NEUSTROEV, V.K. SHAMARDIN, A.V. KOZLOV, Recent developments concerning potential void swelling of PWR internals constructed from austenitic stainless steels. *Proceedings of the Fontevraud V, Contribution of Materials Investigation to the Resolution of Problems Encountered in Pressurized Water Reactors*, Paper No. 22, 2002, p. 23-27.
[40] F.A. GARNER, S.I. POROLLO, YU. V. KONOBEEV, O.P. MAKSIMKIN. Void Swelling of Austenitic Steels Irradiated with Neutrons at Low Temperatures and Very Low dpa Rates. Proc. In: *Proceedings of 12th International Conference on Environmental Degradation of Materials in Nuclear Power systems – Water Reactors*, 2005, p. 439-448.
[41] O.P. MAKSIMKIN, K.V. TSAI, L.G. TURUBAROVA, T. DORONINA, F.A. GARNER. Void Swelling of AISI 321 Analog Stainless Steel Irradiated at Low dpa Rates in the BN-350 Reactor. *Journal of Nuclear Materials,* vol. 367-370, 2007, p. 990-994.
[42] S.I. POROLLO, YU. V. KONOBEEV, A.M. DVORIASHIN, V.M. KRIGAN, F.A. Garner. Determination of the Lower Temperature Limit of Void Swelling of Stainless Steels at PWR-Relevant Displacement Rates. *Proceedings of 10th International Conference on Environmental Degradation of Materials in Nuclear Power Systems – Water Reactor*s, 2002.
[43] S.I. POROLLO, YU. V. KONOBEEV, A.M. DVORIASHIN, A.N. VOROBBJEV, V.M. KRIGAN, F.A. GARNER. Void Swelling at Low Displacement Rates in Annealed 12X18H9T Stainless Steel at 4-56 dpa and 280-332°C, *Journal of Nuclear Materials*, Volume 307-311, 2002, p. 339-342.
[44] TRENTY, D. DEYDIER, Maintenance of the Lower Internal Structures in EDF PWRs. *Proceedings of IAEA Specialists Meeting on Behavior of Core Materials*, Rez, Czech Republic, 6–8 October 1998.

[45] K. FUJII, K. FUKUYA, Irradiation-induced microchemical changes in highly irradiated 316 stainless steel, *Journal of Nuclear Materials*, Volume 469, 2016, p. 82-88.
[46] A. ETIENNE, B. RADIGUET, P. PAREIGE, J.-P. MASSOUD, C. POKOR, Tomographic atom probe characterization of the microstructure of a cold worked 316 austenitic stainless steel after neutron irradiation, *Journal of Nuclear Materials*, Volume 382, Issue 1, 2008, p. 64-69.
[47] A.R. LABORNE, P. GAVOILLE, J. MALAPLATE, C. POKOR, B. TANGUY, Correlation of radiation-induced changes in microstructure/microchemistry, density and thermo-electric power of type 304L and 316 stainless steels irradiated in the Phénix reactor, *Journal of Nuclear Materials*, Volume 460, 2015, p. 72-81.
[48] W. Van RENTERGHEM, A. Al MAZOUZI, S. Van DYCK, Influence of post irradiation annealing on the mechanical properties and defect structure of AISI 304 steel, *Journal of Nuclear Materials*, Volume 413, Issue 2, 2011, p. 95-102.
[49] T. TOYAMA, Y. NOZAWA, W. Van RENTERGHEM, Y. MATSUKAWA, M. HATAKEYAMA, Y. NAGAI, A. Al MAZOUZI, S. Van DYCK. Irradiation-induced precipitates in a neutron irradiated 304 stainless steel studied by three-dimensional atom probe, *Journal of Nuclear Materials*, Volume 418, 2011, p. 62-68.
[50] Z. JIAO, G.S. WAS, Impact of localized deformation on IASCC in austenitic stainless steels, *Journal of Nuclear Materials*, Volume 408, 2011, p. 246–256.
[51] Z. JIAO, J. HESTERBERG, G.S. WAS, Insights into the sources of irradiation hardening in a neutron irradiated 304L stainless steel following post-irradiation annealing, *Journal of Nuclear Materials*, Volume 526, 2019, 151754.
[52] D.J. EDWARDS, F.A. GARNER, S.M. BRUEMMER, P. EFSING, Nano-cavities observed in a 316SS PWR flux thimble tube irradiated to 33 and 70dpa, *Journal of Nuclear Materials*, Volume 384, Issue 3, 2009, p. 249-255.
[53] P. SCOTT, A review of irradiation assisted stress corrosion cracking, *Journal of Nuclear Materials*, Volume 211, 1994, p. 101-122.
[54] P.J. MAZIASZ, D.N. BRASKI, Microstructural design of PCA austenitic stainless steel for improved resistance to helium embrittlement under HFIR irradiation, *Journal of Nuclear Materials*, Volume 122, Issues 1–3, 1984, p. 305-310.
[55] M.L. GROSSBECK, L.K. MANSUR, Tensile and irradiation properties of austenitic stainless steels for first wall alloys for near-term fusion devices, *Materials Science Forum Letters*, Volume 97-99, 1992, p. 407-728.
[56] F.A. GARNER, M.L HAMILTON, L.R. GREENWOOD, J.F. STUBBINS, B.B. OLIVER, Isotopic tailoring with 59Ni to study helium generation rate and their effect on tensile properties of neutron irradiated Fe-Cr-Ni alloys. *Effects of radiation on structural materials*, ASTM-STP, 1175, 1993, p. 921-939.
[57] D. EDWARDS, Radiation-Induced Segregation Behavior in Austenitic Stainless Steels: Fast Reactor versus Light Water Reactor Irradiations. *Proceedings of the 13th International Conference on Environmental Degradation of Materials in Nuclear Power System – Water Reactors*, The Minerals, Metals & Materials Society, 2007.
[58] Z. JIAO, G.S. WAS, Novel features of radiation-induced segregation and radiation-induced precipitation in austenitic stainless steels, *Acta Materialia*, Volume 59, Issue 3, 2011, p. 1220-1238.
[59] B.W. AREY, D.G. ATTERIDGE, S.M. BRUEMMER, Production of Tailored Alloys to Isolate Metallurgical Variables Promoting IASCC, *EPRI*, Palo Alto, CA, 2006.
[60] G. GUPTA, Z. JIAO, A.N. HAM, J.T. BUSBY, G.S. WAS, Microstructural evolution of proton irradiated T91, *Journal of Nuclear Materials*, Volume 351, Issues 1–3, 2006, p. 162-173.

[61] G.S. WAS, Z. JIAO, A. Van der VEN, S. BUREMMER, D. EDWARDS, Aging and Embrittlement of High Fluence Stainless Steels, Final Report, NEUP Project CFP-09-767, *U.S. DOE*, Washington, DC, 2012.
[62] J.F. ZIEGLER, J.P. BIERSACK, SRIM2008 Program, *IBM Corp*, Yorktown, NY, 2008.
[63] Standard Practice for Neutron Radiation Damage Simulation of Charged-particle Irradiation, ASTM Designation E521-89, *Annual Book of ASTM Standards*, Vol. 12.02, American Society for Testing and Materials, Philadelphia, PA, 1989.
[64] G.S WAS, J.T BUSBY, T ALLEN, E.A KENIK, A JENSSON, S.M BRUEMMER, J GAN, A.D EDWARDS, P.M SCOTT, P.L ANDRESON, Emulation of neutron irradiation effects with protons: validation of principle, *Journal of Nuclear Materials*, Volume 300, Issues 2–3, 2002, p. 198-216.
[65] B.H. SENCER, G.S. WAS, M. SAGISAKA, Y. ISOBE, G.M. BOND, F.A. GARNER, Proton irradiation emulation of PWR neutron damage microstructures in solution annealed 304 and cold-worked 316 stainless steels, *Journal of Nuclear Materials*, Volume 323, 2003, p. 18-28.
[66] S.J. ZINKLE, P.J. MAZIASZ, R.E. STOLLER, Dose dependence of the microstructural evolution in neutron irradiated austenitic stainless steel*, Journal of Nuclear Materials*, Volume 206, Issues 2–3, 1993, p. 266-286.
[67] G.S. WAS., T. ALLEN, Radiation-induced segregation in multicomponent alloys: Effect of particle type, Materials Characterization, Volume 32, Issue 4, 1994, p. 239-255.
[68] P.J. MAZIASZ, Overview of microstructural evolution in neutron-irradiated austenitic stainless steels, *Journal of Nuclear Materials*, Volume 205, 1993, p. 118-145.
[69] P.J. MAZIASZ, Formation and stability of radiation-induced phases in neutron-irradiated austenitic and ferritic steels, *Journal of Nuclear Materials*, Volume 169, 1989, p. 95-115.
[70] E.H. LEE, P.J. MAZIASZ, A.F. ROWCLIFFE. *Proceedings of Phase Stability During Irradiation Conference*, J.R. Holland, et al. (Eds.), The Metallurgical Society of AIME, Warrendale, PA, 1981, p. 191–218.
[71] S.J. ZINKLE, 1.03 – Radiation-Induced Effects on Microstructure, Editor(s): Rudy J.M. Konings, *Comprehensive Nuclear Materials*, Elsevier, 2012, p. 65-98.
[72] M. SONG, K. G. FIELD, R. M COX, G. S. WAS, Microstructural characterization of cold-worked 316 stainless steel flux thimble tubes irradiated up to 100 dpa in a commercial Pressurized Water Reactor, *Journal of Nuclear Materials*, Vol. 541, 2020, 152400.